A scanning electron micrograph (SEM) of a microsystem. The background is a dark, textured surface with fine, parallel ridges. Overlaid on this is a prominent, thick, orange-to-yellow meander line that zig-zags across the frame. The line starts as a straight horizontal bar at the top and then forms a series of connected loops and curves. The lighting creates a 3D effect, with highlights on the top edges of the meander line.

nature
electronics

Microsystems compress for success

Three-dimensional piezoelectric polymer microsystems for vibrational energy harvesting, robotic interfaces and biomedical implants

Mengdi Han^{1,14}, Heling Wang^{1,2,3,4,14}, Yiyuan Yang³, Cunman Liang^{1,5}, Wubin Bai^{1,2}, Zheng Yan⁶, Haibo Li^{4,7}, Yeguang Xue^{2,3,4}, Xinlong Wang⁸, Banu Akar⁸, Hangbo Zhao¹, Haiwen Luan^{2,3,4}, Jaeman Lim¹, Irawati Kandela⁹, Guillermo A. Ameer^{8,10,11}, Yihui Zhang^{12*}, Yonggang Huang^{1,2,3,4*} and John A. Rogers^{1,2,3,8,11,13*}

Piezoelectric microsystems are of use in areas such as mechanical sensing, energy conversion and robotics. The systems typically have a planar structure, but transforming them into complex three-dimensional (3D) frameworks could enhance and extend their various modes of operation. Here, we report a controlled, nonlinear buckling process to convert lithographically defined two-dimensional patterns of electrodes and thin films of piezoelectric polymers into sophisticated 3D piezoelectric microsystems. To illustrate the engineering versatility of the approach, we create more than twenty different 3D geometries. With these structures, we then demonstrate applications in energy harvesting with tailored mechanical properties and root-mean-square voltages ranging from 2 mV to 790 mV, in multifunctional sensors for robotic prosthetic interfaces with improved responsivity (for example, anisotropic responses and sensitivity of 60 mV N⁻¹ for normal force), and in bio-integrated devices with in vivo operational capabilities. The 3D geometries, especially those with ultralow stiffnesses or asymmetric layouts, yield unique mechanical attributes and levels of functionality that would be difficult or impossible to achieve with conventional two-dimensional designs.

Thin-film devices in planar architectures are the basis for entire classes of technologies in flexible electronics/optoelectronics^{1,2}, biomedical devices^{3,4}, energy storage and conversion systems^{5–8}, and micro/nanoelectromechanical systems^{9,10}. Piezoelectric devices, which include mechanical sensors^{11–13}, ultrasonic transducers^{14,15}, energy harvesters^{16,17}, and robots and actuators^{18,19} adopt many of the same types of planar, multilayer layouts and device design strategies. Progress in such systems relies on advances in the materials chemistry of inorganic ceramics, organic polymers^{20,21}, two-dimensional (2D) materials^{22,23} and biologically derived systems^{24,25}, with a focus on developing enhanced piezoelectric properties such as the voltage/charge coefficient and electromechanical coupling factor^{26–28}. Progress in these systems also relies on structural designs^{29–31} to develop optimized responses or unusual characteristics such as curvilinear shapes or stretchable mechanics. Such work is currently constrained by thin-film deposition, growth, etching and lithographic patterning techniques, which allow access only to 2D multilayer configurations and, by extension, simple, macroscopic three-dimensional (3D) geometries³². Deterministic assembly

of piezoelectric material structures and device components into complex, 3D mesoscale architectures could provide valuable additional options in engineering design, as potential routes to unique properties and/or functions that would otherwise be difficult or impossible to achieve.

Among various strategies in 3D microfabrication^{33–35}, methods that use compressive buckling associated with forces imparted by soft, elastomeric substrates are particularly attractive. These techniques operate in a high-speed, parallel fashion on devices and structures that combine the most advanced functional materials in the most sophisticated 2D configurations, simultaneously across length scales that range from nanometres to metres^{36–41}. In this Article, we apply these methods to 2D, thin-film piezoelectric devices, creating 3D microsystems with advanced capabilities in sensing and energy harvesting through more than 20 different structures. Integration of passive components (for example, electrodes, encapsulation layers, proof mass) and the use of additional concepts in sacrificial support features allows access to 3D functional devices with ultralow stiffnesses, which are of interest in mechanical sensing and harvesting in

¹Center for Bio-Integrated Electronics, Northwestern University, Evanston, IL, USA. ²Department of Materials Science and Engineering, Northwestern University, Evanston, IL, USA. ³Department of Mechanical Engineering, Northwestern University, Evanston, IL, USA. ⁴Departments of Civil and Environmental Engineering, Northwestern University, Evanston, IL, USA. ⁵Key Laboratory of Mechanism Theory and Equipment Design of Ministry of Education, School of Mechanical Engineering, Tianjin University, Tianjin, China. ⁶Departments of Biomedical, Biological & Chemical Engineering, Mechanical and Aerospace Engineering, University of Missouri, Columbia, MO, USA. ⁷School of Naval Architecture, Ocean and Civil Engineering (State Key Laboratory of Ocean Engineering), Shanghai Jiaotong University, Shanghai, China. ⁸Department of Biomedical Engineering, Northwestern University, Evanston, IL, USA. ⁹The Center for Developmental Therapeutics, Northwestern University, Evanston, IL, USA. ¹⁰Department of Surgery at Northwestern University Feinberg School of Medicine, Chicago, IL, USA. ¹¹Center for Advanced Regenerative Engineering, Northwestern University, Evanston, IL, USA. ¹²Center for Flexible Electronics Technology and Center for Mechanics and Materials; AML, Department of Engineering Mechanics, Tsinghua University, Beijing, China. ¹³Departments of Neurological Surgery, Chemistry, Electrical Engineering and Computer Science; and Simpson Querrey Institute for BioNanotechnology, Northwestern University, Evanston, IL, USA. ¹⁴These authors contributed equally: Mengdi Han, Heling Wang. *e-mail: yihuzhang@tsinghua.edu.cn; y-huang@northwestern.edu; jrogers@northwestern.edu

the context of soft biological systems and low-frequency responses. Our experimental measurements of these devices, together with theoretical and finite element analysis (FEA) of their assembly and operation, highlight their capabilities in multidirectional energy conversion, broadband operation and multifunctional sensing.

Piezoelectric microsystems in 3D formats

Figure 1a shows an exploded view schematic illustration and a scanning electron microscope (SEM) image of a representative 3D piezoelectric microsystem that includes a layer of piezoelectric polymer (polyvinylidene difluoride, PVDF, with thicknesses of 13 μm and 28 μm in thin and thick regions, respectively) and layers of metal (Cr/Au, 10 nm/100 nm in thickness) as electrodes on the top and bottom surfaces. Here, the thick region consists of an extra layer of PVDF. This design provides a spatial variation of bending stiffness in the 2D precursor, thereby yielding engineered folds at desired locations during the compressive buckling. The scheme for forming this structure begins with the use of a set of techniques in planar microfabrication (that is, photolithography, wet/dry etching) to define a 2D precursor structure. Transfer printing onto a pre-strained elastomer leads to bonding at lithographically defined sites, such that release of the pre-strain geometrically transforms the system into a well-defined resultant 3D architecture (Supplementary Fig. 1). The thin regions of PVDF lead to the formation of ‘folds’ at these locations. Additional details appear in the Methods and in Supplementary Note 1. Such strategies establish routes to 3D piezoelectric microsystems with diverse geometries defined by the 2D precursor, the configuration and magnitude of the pre-strain in the elastomer substrate, and the bonding locations. Examples include 3D mesostructures that incorporate narrow filaments, plates/membranes, continuously curved features, sharp folds, single or multiple levels of hierarchy in 3D shapes and feature sizes, in multilayered configurations of active or passive materials (Fig. 1b and Supplementary Figs. 2–6).

Active, piezoelectric systems represent the focus of the work presented here. In some examples in energy harvesting and related applications, structures with ultralow effective stiffnesses are of interest. Methods that achieve 3D mesostructures by controlled mechanical buckling, as described above, do not provide access to the necessary geometries, however, due to requirements for bending stiffnesses sufficient to enable the assembly process. Schemes introduced here avoid this limitation by the use of temporary structural supports designed to drive the buckling motions of associated 3D piezoelectric structures with ultralow bending stiffnesses (that is, typically more than one order of magnitude smaller than that of conventional 3D mesostructures; see Supplementary Fig. 7). As shown in Fig. 1c, the process begins with simultaneous buckling of a bilayer 2D precursor. In this example, a ribbon of polyimide (PI; 12.5 μm in thickness) serves as an underlying support layer for a thin structure of PVDF (9 μm in thickness) in a low-stiffness, serpentine shape. During the assembly process, the PI ribbon, bonded at its two ends to an elastomer substrate (700 μm in thickness, pre-strain of 10%), buckles upwards, thereby imparting forces onto the back side of the PVDF serpentine to induce out-of-plane motions and a resulting 3D shape (Supplementary Fig. 8). Selectively releasing the bonding sites of the PI ribbon allows for its removal, thereby leaving an ultralow-stiffness serpentine in a 3D geometry. Without the PI, releasing the prestrain yields a serpentine with a largely 2D, wrinkled geometry because the stiffness of the structure is unable to overcome the forces of non-specific adhesion (that is, Van der Waals forces) between it and the underlying elastomer (Supplementary Fig. 9). Specifically, quantitative energetic calculations based on FEA (see Supplementary Note 2 for details) suggest that without the temporary supporting layer, the local buckling state (Supplementary Fig. 10b) in which the serpentine adheres to the substrate is more energetically favourable than the global buckling

state (Supplementary Fig. 10c), due to the adhesion energy and the low stiffness of the serpentine mesostructure. (In contrast, the straight ribbon geometry of the supporting layer yields a comparatively much larger stiffness, even for the case of similar thicknesses, thereby enabling delamination from the elastomer to yield an arch shape⁴².) This process induces transformation of the serpentine into a 3D configuration. Subsequently, the supporting layer collapses to the substrate in a very short period of time (~ 0.3 ms, Supplementary Fig. 11a) upon detaching its bonding sites. After removing the supporting layer, this global buckling state remains, as it corresponds to a state of local energy minimum. Numerical examples of this energetic analysis appear in Supplementary Note 3 and Supplementary Figs. 10 and 11.

Subsequent stretching of the elastomer allows the ultralow-stiffness 3D mesostructures to shift back to their original 2D planar shapes. Different from the buckling process, which requires an intimate contact between the fractal curves, the supporting layer and the underlying elastomer, the stretching process can yield only comparatively poor contact and lower adhesion between the fractal curves and the elastomer due to surface roughness⁴³. The ultralow-stiffness 3D mesostructures can, therefore, switch between 2D and 3D geometries through stretching and releasing of the elastomer (Supplementary Fig. 12). Examples of ultralow-stiffness 3D mesostructures formed in this manner in PVDF (9 μm in thickness, 20 μm in ribbon width) include simple fractal curves (the left frame in Fig. 1d,e, stiffness: 0.26 N m^{-1}), and those with two orders (the middle frame in Fig. 1d,e and Supplementary Fig. 13, stiffness: 0.18 N m^{-1}) and Hilbert geometries (the right frame in Fig. 1d,e, stiffness: 0.084 N m^{-1}). The good agreement between FEA (Fig. 1d) and experimental results (Fig. 1e) highlights the level of control and reproducibility that is possible. These concepts expand the range of design opportunities in low-stiffness 3D structures beyond those possible with previously published schemes.

Energy harvesting from 3D piezoelectric microsystem

Such classes of ultralow-stiffness 3D mesostructures in functional piezoelectric materials offer complex modes of motion induced by vibrations, thereby creating interesting opportunities in energy harvesting, especially for small-scale systems. Figure 2a–d and Supplementary Figs. 14a and 15–16 feature an array of 3D serpentine structures as an example that is engineered for multidirectional energy harvesting. This device consists of PVDF (9 μm in thickness, 50 μm in ribbon width, 3 mm in lateral dimension, 1.2 mm in vertical displacement) with top (Cr/Au/Ti, 10 nm/100 nm/20 nm in thickness) and bottom (Cr/Au, 10 nm/100 nm in thickness) electrodes, as shown in the inset in Fig. 2a and Supplementary Fig. 14a. Harmonic vibrations can excite selected vibrational modes of the 3D structure, thereby producing electrical power that can be harvested through contacts to the metal electrodes. For out-of-plane vibrations (that is, vertical direction; peak accelerations of 4g), the device generates root-mean-square (RMS) voltages over 1 mV between 600 Hz to 700 Hz (Fig. 2a). Unlike traditional harvesters that use simple cantilever geometries, the 3D serpentine configuration enables operation for motions in multiple directions. For example, Fig. 2b shows that in-plane vibrations (that is, lateral direction) induce comparable electrical outputs. In both cases, the peak output RMS voltage (2.02 mV under out-of-plane vibration, 1.73 mV under in-plane vibration) occurs at ~ 650 Hz. Figure 2c presents the time dependence of the output voltage and corresponding fast Fourier transform (FFT). The single, well-defined peak at ~ 657 Hz is consistent with a linear mechanical response. The resonance lies in the midrange of the audible spectrum, thereby creating opportunities in harvesting energy from the sounds of the human voice, musical instruments and ambient noise. Figure 2d shows an example of converting sound (657 Hz) from a commercial speaker (Logitech, S-150) into electrical power. The feature of multidirectional energy

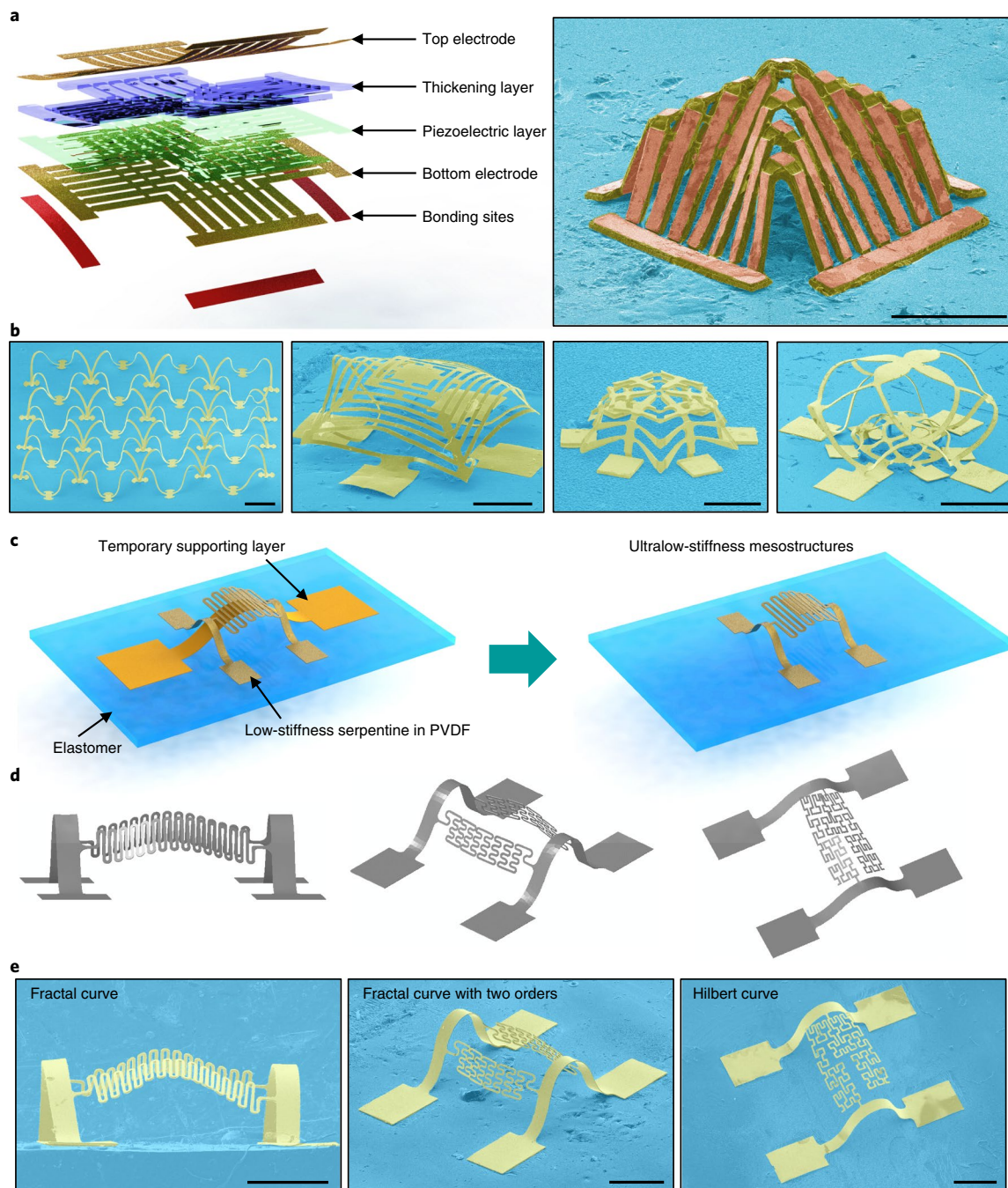


Fig. 1 | 3D mesoscale piezoelectric frameworks and ultralow-stiffness mesostructures. **a**, Exploded-view schematic illustrations (left) and SEM image (right) of a 3D PVDF mesostructure with top and bottom metal electrodes. **b**, SEM images of representative 3D mesoscale networks in PVDF, including an array of filamentary serpentine (left), mixed collection of membranes and filaments (middle left), folded sheets (middle right), and overlapping networks (right). **c**, Process for assembly of mesostructures with ultralow stiffnesses. **d,e**, FEA predictions (**d**) and corresponding SEM images (**e**) of ultralow-stiffness PVDF mesostructures, including examples that consist of first- (left) and second-order (middle) fractal curves and a Hilbert geometry (right). Scale bars, 500 μm .

harvesting allows the device to operate independently of the relative position between the device and the speaker. Regions I, II and III in Fig. 2d correspond to locating the speaker next to the device, gradually changing the position of the speaker, and placing the speaker above the device, respectively.

Broadband operation is advantageous for many applications in energy harvesting. Figure 2e–h shows a design configured towards this goal. The structure involves a buckled bi-stable serpentine (PVDF, 9 μm in thickness, 50 μm in ribbon width) and a proof mass

(Cu, 500 $\mu\text{m} \times 500 \mu\text{m} \times 500 \mu\text{m}$). The overall lateral dimensions are 3 mm \times 3 mm and the height is 1.5 mm (the inset in Fig. 2e and Supplementary Fig. 14b). Here, the buckled shape provides two stable states, with a serpentine layout that, together with the proof mass, reduce the energy barrier between these two states, thereby facilitating the excitation of nonlinear vibrational responses. As such, under an out-of-plane vibration with an acceleration of 4g, this 3D system can generate electrical power across a range of frequencies spanning two orders of magnitude (that is, from 5 Hz to

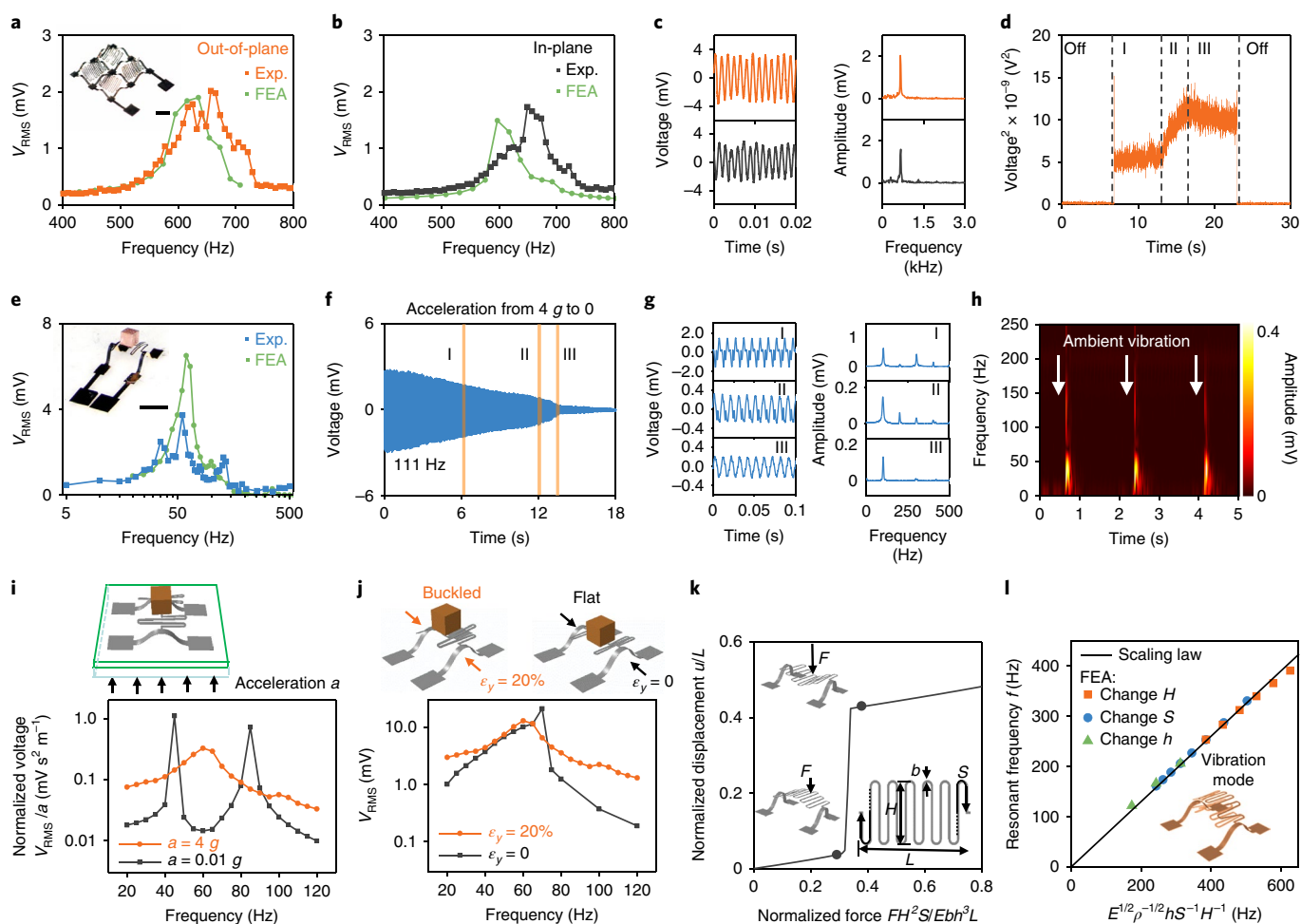


Fig. 2 | 3D vibratory piezoelectric energy harvesters. **a–c**, Electrical output characteristics of a 3D serpentine array for multidirectional energy harvesting, including RMS voltages at different frequencies for out-of-plane (**a**) and in-plane (**b**) vibrations, with time-domain output voltage and fast Fourier transform results (**c**) that highlight a resonance at 657 Hz. **d**, Power spectrum of the 3D serpentine array when excited at 657 Hz with a commercial speaker. The inset in **a** features an optical image of the device. **e**, RMS voltages from a bi-stable 3D serpentine structure with an integrated test mass for broadband energy harvesting. **f, g**, Time-domain output voltage from a bi-stable 3D serpentine structure at 111 Hz under different accelerations (**f**), with a magnified view and fast Fourier transform (**g**). **h**, Spectrogram of the output voltage associated with periodic ambient vibration. The inset in **e** shows an optical image of the device. **i**, FEA prediction of the dependence of the normalized open-circuit voltage (RMS) on frequency in a regime of nonlinear (acceleration 4 g) and linear (acceleration 0.01 g) vibratory response. **j**, FEA prediction of the dependence of the open-circuit voltage (RMS) on frequency for a buckled and flat serpentine pattern. **k**, Scaling law for the relationship between the nonlinear normalized displacement and the normalized force for the buckled serpentine pattern. **l**, Scaling law for the resonant frequency of the buckled serpentine pattern ($\epsilon_y = 10\%$). The solid line in **l** is a linear fit to the data. Scale bars, 1 mm.

500 Hz, Fig. 2e). Supplementary Fig. 17 summarizes representative time-domain output voltages with corresponding FFT analyses. Figure 2f presents the voltage under different accelerations. The magnified view and corresponding fast Fourier transform (FFT) in Fig. 2g illustrate the transition from nonlinear to linear response as the vibratory acceleration decreases in magnitude. A device with this construction has, by extension, the ability to harvest energy from broadband ambient vibrations. As an example, an impulsive force delivered to the supporting surface of this type of device induces damped vibrations of the serpentine, thereby generating electrical power with gradually decreased amplitude. Figure 2h shows the spectrogram of the output voltage produced by periodic delivery of the force. The corresponding time-domain output voltage appears in Supplementary Fig. 18. A lower level of vibrations with an acceleration of 0.1 g is also detectable by introducing filters to reduce the noise (Supplementary Fig. 19).

FEA further demonstrates that these nonlinear responses lead to capabilities in energy harvesting that extend over a much broader

range of frequencies than that possible with a linear response. As shown in Fig. 2i, the frequency spectrum of the normalized output voltage shows peaks at discrete values during linear vibrations. By contrast, the large output voltages extend over a comparatively wide frequency range during nonlinear vibrations. Furthermore, the 3D serpentine formed via controlled buckling has a notably larger output voltage than that of the 2D serpentine over a wide range of frequencies, as shown by the FEA result in Fig. 2j and experimental results in Supplementary Fig. 20. The full-width at half-maximum values are about 30 Hz and 18 Hz for the bi-stable 3D serpentine and flat 2D serpentine, respectively.

These classes of 3D piezoelectric energy harvesters clearly offer mechanical properties that are beneficial in vibrational energy harvesting. Many other designs with tailored mechanical properties are also possible. Supplementary Figs. 14c and 21, 22 highlight a 3D spiral piezoelectric device in a multilayer format. Key considerations for this device include a spiral shape that reduces its stiffness and a 3D geometry that provides space for large-amplitude vibrations.

The result is an energy harvester with a low resonant frequency and a wide operating frequency range (Supplementary Fig. 21), with the ability to harvest energy from air flow (Supplementary Fig. 22). This geometric diversity creates possibilities for designs specifically tailored to application requirements.

Further refinements in layout can lead to an improved output of 3D vibratory energy harvesters while retaining their unique mechanical properties (for example, low resonant frequency, wide bandwidth), thereby creating opportunities for their use in practical applications. For example, adding a PI supporting layer (Supplementary Fig. 23) increases the open-circuit output voltage by two orders of magnitude, due mainly to the offset of the PVDF relative to the neutral mechanical plane, leading to an increased membrane strain during bending deformations. The open-circuit output voltage can also be improved by optimizing the pattern of the electrode (Supplementary Fig. 24b). Based on guidance from FEA results for the spatial distribution of voltage (without electrodes; Supplementary Fig. 24c), the electrode can be designed to cover regions of positive voltage and to avoid those with negative voltage. The result increases the net output voltage by a factor of 2.2 (Supplementary Fig. 24d). Experimental examples of using a supporting layer and patterned electrode to enhance the output voltages appear in Supplementary Figs. 25–27. A 3D bi-stable serpentine structure with larger dimensions and patterned electrode can produce an RMS voltage around 0.79 V (Supplementary Fig. 26).

Fundamental studies of energy harvesting

As highlighted in the previous sections, broadband vibrational energy harvesting results from nonlinear deformations due to the combined effect of ultralow-stiffness serpentine microstructures and compressive buckling. A platform that allows further study of the underlying physics involves a buckled serpentine pattern as shown in Supplementary Fig. 28, where an applied force (F) serves as an external mechanical stimulus. When the magnitude of this force increases beyond a critical point (F_c), the serpentine switches from a geometry with negative vertical curvature to one with positive curvature, leading to a highly nonlinear displacement–force relation (Fig. 2k). The following scaling law captures the relationship among the displacement (u), force (F) and the geometry/material parameters for this case

$$\frac{u}{L} = U \left(\frac{FH^2S}{Ebh^3L} \right) \quad (1)$$

where L , H , b and S are the serpentine length, height, width and total arc length, respectively; h is the thickness, E is the material Young's modulus and U is a nonlinear function that depends on the compressive strain (ϵ_y) applied to the serpentine pattern during compressive buckling. When the compressive strain $\epsilon_y = 0$, the $\frac{u}{L}$ versus $\frac{FH^2S}{Ebh^3L}$ relationship is almost linear (Supplementary Fig. 29), due to the flat, 2D geometry of the serpentine in this situation. The 3D shape of the serpentine pattern formed via compressive buckling is, in this sense, crucial in realizing nonlinear deformations. The scaling law is consistent with FEA for typical serpentine geometries (with $L \ll S$ and $h \ll b$), as shown in Supplementary Fig. 30 and Supplementary Note 4.

The ultralow-stiffness serpentine pattern allows nonlinear deformations to follow from forces with small magnitudes. For a representative set of geometric and material parameters, $L = H = 1$ mm, $S = 10L$, $h = 9 \mu\text{m}$, $b = 50 \mu\text{m}$, $E = 2$ GPa (PVDF) and $\epsilon_y = 10\%$, the scaling law equation (1) indicates that the critical force required to actuate nonlinear deformations can be as low as $2 \mu\text{N}$, in a range accessible to biological stimuli such as the beating of muscle cells^{44,45}. By comparison, a straight ribbon with otherwise similar geometries and materials requires a force with a magnitude ~ 250 times larger

than this value to actuate nonlinear deformations, according to FEA (Supplementary Fig. 31).

The scaling law in equation (1) also suggests that the serpentine pattern has a low resonant frequency, because of its low stiffness. The stiffness, defined as $K = \frac{\partial F}{\partial u} \Big|_{u=0}$, is linearly proportional to $\frac{Ebh^3}{H^2S}$ (see FEA validation in Supplementary Fig. 32 and Supplementary Note 4). Dimensional analysis suggests that the equivalent mass of vibration (M) is linearly proportional to ρbhS , where ρ is the material density. Therefore, the linear resonant frequency (f) obeys the scaling law,

$$f = \alpha \sqrt{\frac{K}{M}} = \alpha \frac{h}{HS} \sqrt{\frac{E}{\rho}} \quad (2)$$

where α is a dimensionless constant that depends on the vibration mode and the compressive strain ϵ_y . With $\alpha = 0.65$, this relationship agrees reasonably well with FEA results for the first-order vibrational mode, as shown in Fig. 2l ($\epsilon_y = 10\%$). Additional details concerning the validation of equation (2) are in Supplementary Fig. 33 and Supplementary Note 4. For representative parameters, $H = 2$ mm, $S = 15H$, $h = 9 \mu\text{m}$, $E = 2$ GPa and $\rho = 1800 \text{ kg m}^{-3}$, the resonant frequency is below 100 Hz. By comparison, at similar length scales and with similar materials, 3D structures without this type of serpentine geometry typically have resonant frequencies larger than 10 kHz (ref. 46). The serpentine design is an important, enabling aspect of efficient energy harvesting from low-frequency mechanical stimuli, such as machine-induced vibrations (10–100 Hz)⁴⁷ and human motions (< 10 Hz)⁴⁸.

3D piezoelectric microsystems as robotic interfaces

In addition to vibrations, other types of mechanical stimuli such as pressure, normal force, stretching and bending from biological or environmental sources can induce responses. Designs that operate effectively in such cases can broaden uses in energy harvesting and expand applications to mechanical sensing (Fig. 3 and Supplementary Figs. 34–40). Figure 3a,b presents exploded schematic illustrations and optical images of a representative 3D device. Here, the 3D geometry offers an increased number of degrees of freedom in deformation compared to 2D alternatives, thereby creating interesting design possibilities. Encapsulating these 3D structures with a soft silicone elastomer (1 mm in thickness, Ecoflex, Smooth-On) physically protects the device, while maintaining its deformability (the middle frame in Fig. 3b).

Figure 3c–f and Supplementary Fig. 37 present some results for application of normal forces (pressing) over large and small areas. The large area (1 cm by 1 cm) case can lead to global deformation of the 3D piezoelectric structure (the top frame in Fig. 3c)⁴⁹, thereby generating peak voltages > 1 V (RMS voltage ~ 350 mV) when the magnitude of the force is 32 N. Measurable output occurs for forces as small as 30 mN. The output RMS voltage changes with the magnitude of the force (Fig. 3e), with high sensitivity (60 mV N^{-1}) at small forces (that is, forces below 3 N) and comparatively low sensitivity (5.7 mV N^{-1}) at large forces (that is, forces above 3 N) due to the increased slope of the stress-strain response of the elastomer⁵⁰. The encapsulation materials and the 3D geometries can be selected for desired sensitivity. Forces applied over small areas induce only local deformations. Controlling the displacement of a cylinder with a diameter of 0.65 mm yields forces over a small circular region with magnitudes from 0 to 91 mN (Supplementary Fig. 38). Here, asymmetric designs (the right frame in Fig. 3b and Supplementary Fig. 34) allow the position of the applied force to be determined from the shape of the output signal. Figure 3f shows the time-domain output voltage in the case of application of force over a small circular region (diameter: 0.65 mm, displacement of the cylinder: 1 mm) at five different positions. Such distinct response shapes in these five cases

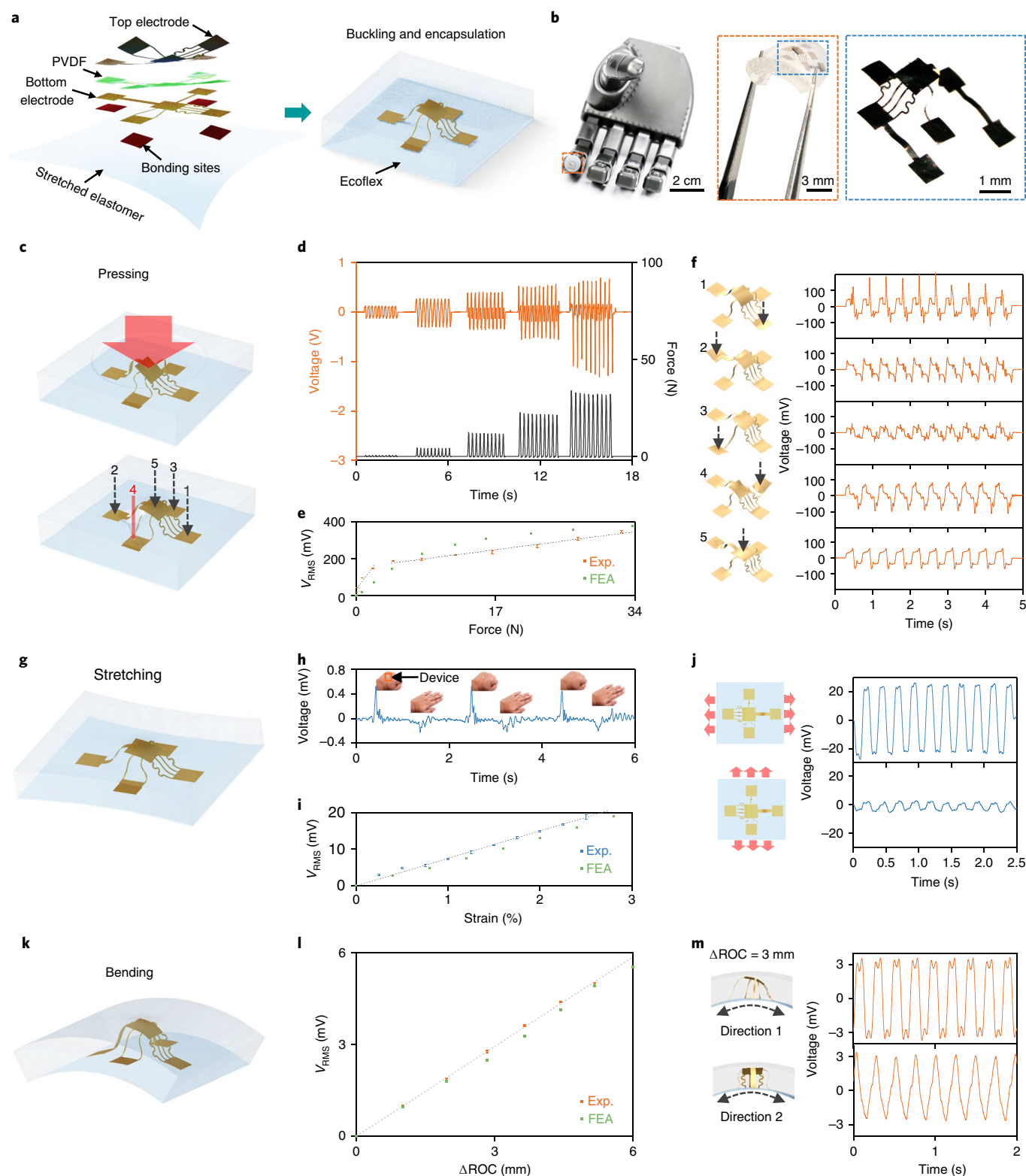


Fig. 3 | Impact-based 3D piezoelectric energy harvester and sensors. **a**, Exploded view of the 2D geometry (left) and schematic illustration of the impact-based 3D piezoelectric energy harvester (right). **b**, Optical images of the device attached to a robotic arm (left), the encapsulated device (middle), and the 3D geometry before encapsulation (right). **c**, Schematic illustration of the device under pressure applied over a large area (top) and a small area (bottom). **d**, Time-domain output voltage (orange curve) with different external forces (dark grey curve) applied over a square area (1 cm²). **e**, The dependence of RMS voltage on the applied force. **f**, Time-domain output voltage with external forces applied over different small circular regions (0.65 mm in diameter). **g**, Schematic illustration of the device under stretching. **h**, Demonstration of harvesting mechanical energy from human skin by attaching the device onto the dorsal surface of a hand. **i**, Dependence of RMS voltage on the applied strain. **j**, Time-domain output voltage with strains applied in different directions. **k**, Schematic illustration of the device under bending. **l**, Dependence of RMS voltage on the change of radius of curvature at different bending directions. **m**, Time-domain output voltage by bending along different directions. Error bars in **e**, **i** and **l** correspond to the calculated standard error deviation from three measurements. Grey dashed lines are linear fits to the data.

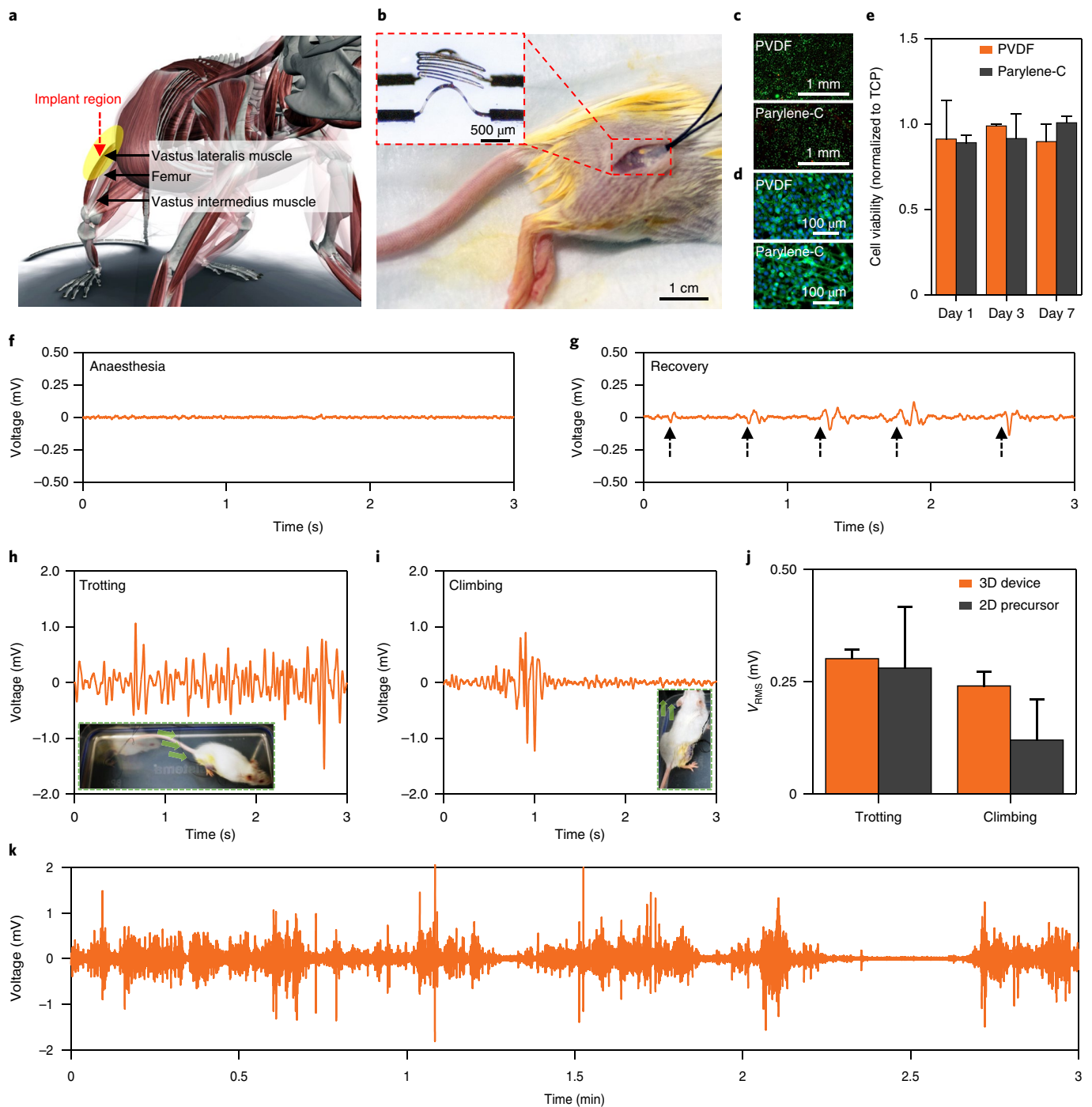


Fig. 4 | 3D piezoelectric devices as biomedical implants. **a**, Schematic illustration of the location of a subdermal implant. **b**, Optical image of a 3D piezoelectric energy harvester implanted into the hind leg of a mouse. The inset shows a magnified optical image of the device. **c**, Representative fluorescence images from a cytotoxicity assay (live/dead test) for fibroblasts after three days of culturing on PVDF and parylene-C. Green indicates live cells and red indicates dead cells. **d**, Representative fluorescence images from F-actin staining for fibroblasts after seven days of culturing on PVDF and parylene-C. Green indicates actin filaments and blue indicates cell nuclei. **e**, Normalized cell viability data based on alamar blue assay for days 1, 3 and 7, proving no signs of cytotoxicity for all the groups. Error bars correspond to the calculated standard error deviation from three measurements. **f**, Output voltage of the 3D piezoelectric device when the mouse is anaesthetized. **g**, Output voltage when the mouse begins to recover but shows no obvious movement. **h,i**, Output voltage under different mouse behaviours: trotting (**h**), climbing (**i**). Insets show corresponding images of the mouse behaviour. **j**, Comparison of the output voltage from the 3D device and its 2D precursor under different behaviours of the animal. Data correspond to averages of five different trotting and climbing behaviours. Error bars correspond to calculated standard error deviation. **k**, Output voltage of the 3D piezoelectric device as the mouse freely moves inside an enclosure for three minutes.

can be attributed to the different types of associated deformations, as illustrated in the left frame of Fig. 3f. As the displacement of the cylinder decreases to 0.75 mm, the differences in response shapes

become less obvious. Smaller displacements (for example, 0.5 mm and 0.25 mm) yield similar responses for different pressing positions (Supplementary Fig. 39). Other types of 3D mesostructures,

including but not limited to those with filaments and membranes, are also feasible for energy harvesting and sensing of normal pressure (Supplementary Fig. 40).

Figure 3g–j presents a schematic diagram and the results of energy harvesting from uniaxial stretching, a mode of deformation that can be relevant for interfaces to biomechanical sources of motion. An example is in adhesive integration (Silbione RT Gel 4717 A/B, Bluestar Silicones) of a device on the skin. Figure 3h shows that a device attached on the dorsal surface of the hand produces a peak voltage > 0.5 mV as the gesture switches between closed fist and open hand. The linear relationship between the RMS voltage and applied strain provides the basis for sensing of strain (Fig. 3i). The asymmetric design allows determination of the direction of stretching from the amplitudes of the output signals if the value of the applied uniaxial strain is known. For example, under the same strain of 2.5%, the RMS voltage along two directions differs by more than a factor of seven (that is, 18.5 mV and 2.5 mV), as shown in Fig. 3j.

A bending mode of operation is also possible (Fig. 3k–m). Changes in the radius of curvature (Δ ROC) define the mechanical stimulus in this case. Increasing the magnitude of this change increases the output voltage in a linear fashion (Fig. 3l). Different directions of bending also result in distinguishable amplitudes in the electrical response (Fig. 3m). For example, bending at a Δ ROC of ~ 3 mm along direction 1 and direction 2 (illustrated in the left frame of Fig. 3m) leads to RMS voltages of 2.8 mV and 2.1 mV, respectively. A key appealing aspect of this 3D piezoelectric device is that the amplitudes of its output voltage change with the magnitude as well as the direction of the mechanical stimuli, and the shapes of its output signals vary with the location and type of mechanical stimuli, with corresponding capabilities in detection. Examples include, but are not limited to, distinguishing the positions of an applied force by comparing the shapes of the output signal (Fig. 3f) and measuring the intensity or direction of uniaxial strain based on the amplitude of the output voltage (Fig. 3i,j). These additional options in mechanical sensing suggest potential routes for developments of robotic prosthetic interfaces. Further integrating multiple devices over a large area in a distributed manner allows for gesture recognition, spatio-temporal mapping of motions, and other applications.

Implantation of 3D piezoelectric microsystems

These 3D piezoelectric systems are well configured for interactions with biological systems, in three dimensions. One example involves implantation in a region in the hind leg of a female mouse, as illustrated in Fig. 4a,b. Here, a conformal coating of parylene-C (2 μ m in thickness) encapsulates the 3D device (the inset in Fig. 4b) to prevent the penetration of biofluids. Figure 4c–e and Supplementary Fig. 41 support biocompatibility of the encapsulation layer and the functional piezoelectric material (PVDF, 9 μ m in thickness). Specifically, fibroblast cells show no signs of cytotoxicity when cultured on films of PVDF or parylene-C for up to three days (Fig. 4c); they remain adhered to the surface with appropriate morphology after seven days (Fig. 4d). Observations indicate no significant differences in cell viability among tissue culture plastic (TCP), PVDF and parylene-C groups (Fig. 4e).

After implantation, the device shows no output signal (Fig. 4f) until the mouse gradually recovers from anaesthesia and begins with small movements, yielding small voltages of ~ 100 μ V (Fig. 4g). Following complete recovery, the mouse exhibits normal locomotor activity inside an enclosure (23 cm by 16 cm in area, 16 cm in height), including but not limited to trotting and climbing. Such motion induces output voltages with peak amplitudes > 1 mV (Fig. 4h,i). Here, the 3D geometry allows the device to deform easily under external forces, thereby enabling efficient coupling to contractile motions of surrounding muscles without irritation or significant mechanical constraints on natural movements. By comparison, the

corresponding 2D counterpart (Supplementary Fig. 42) implanted at the same region exhibits reduced stability and output performance. Specifically, the output voltage of the 2D precursor under trotting behaviour has a comparable amplitude to the corresponding 3D device, although its output under climbing behaviour is lower (Fig. 4j). In both cases, the 2D precursor fails to produce output signals with repeatable amplitudes, due to insufficient deformation in certain cases (Supplementary Fig. 43 and Supplementary Video 1). For example, similar trotting behaviours can result in RMS voltages that span one order of magnitude (that is, from 0.04 mV to 0.4 mV). Figure 4k and Supplementary Video 2 illustrate the stability of output signals from the 3D piezoelectric device with a mouse moving freely inside the enclosure. The device can still produce electrical signals under trotting behaviours after implantation for ~ 48 hours (Day 3, Supplementary Fig. 44). FEA study of typical types of deformation further supports the use of the device in this application. Under pressure, the output voltage is larger than that of the 2D precursor by one order of magnitude (Supplementary Fig. 45a), because the underlying dermis constrains the deformation of the 2D structure. Under bending deformation, the output voltages of the 2D and 3D devices are of the same order of magnitude (Supplementary Fig. 45b). Consistency between the output amplitude and motion intensity suggests the feasibility of using such 3D piezoelectric microsystems as biomedical implants for energy harvesting and sensing.

Conclusions

Our results provide pathways for extending piezoelectric microsystems to three dimensions in a collection of architectures that are configured for applications in energy harvesting, robotic prosthetic interfaces and biomedical implants. The experimental results, computational models and theoretical studies reveal the possibilities of using 3D piezoelectric microsystems for multidirectional, broadband and/or low-frequency energy harvesting from vibrations of various types; for mechanical to electrical energy conversion from a wide range of applied forces; for sensing the intensity and distinguishing the direction/position of mechanical stimuli; and for in vivo biomechanical energy harvesting and sensing. Our mechanically guided 3D assembly approach allows 3D piezoelectric microsystems to leverage the most advanced micro/nanofabrication techniques and sophisticated active materials, in a diverse set of 3D geometries. The structures can offer ultralow-stiffness and asymmetric designs, as well as controlled thickness profiles, coherently coupled multilayers, selective bonding configurations and gradient arrays that result from non-uniform distributions of prestrain.

Methods

Fabrication of 3D piezoelectric mesostructures. Preparation of 2D precursors in PVDF began with spin coating (1,000 r.p.m. for 60 s) and curing (70 °C for 1 h) polydimethylsiloxane (PDMS) (1:10, Sylgard 184, Dow Corning) on silicon wafers. Laminating a film of PVDF (9 μ m in thickness, Piezotech) onto these substrates and depositing Cr/Au (5 nm/50 nm in thickness) via electron beam evaporation formed a hard mask for patterning the PVDF by dry etching with O_2 . Next, photolithography defined a pattern of resist (AZ 5214E, MicroChem) for wet etching of the Cr/Au and dry etching of PVDF, to complete the fabrication of the 2D precursor structures. After removing the hard mask (Cr/Au), a piece of poly(vinyl alcohol) (PVA) tape allowed retrieval of the PVDF structures from the PDMS-coated wafer to expose their back sides for deposition of Ti/SiO₂ (10 nm/100 nm in thickness) via electron beam evaporation through a shadow mask to serve as the bonding sites. The process of compressive buckling began with stretching of a flat silicone elastomer substrate using a custom mechanical stage. Exposing the 2D structures and the surface of this elastomer (Dragon Skin, Smooth-On) to ultraviolet-induced ozone created chemical functionalization to facilitate bonding. Laminating the 2D precursors/PVA tape onto the stretched elastomer and then heating at 70 °C for 10 min led to the formation of strong siloxane bonds at the bonding sites. Dissolving the PVA with water and releasing the prestrain transformed the 2D precursors into 3D mesostructures.

Fabrication of 3D folded piezoelectric mesostructures. The process began by laminating a film of PVDF (28 μ m in thickness, TE Connectivity) onto PDMS-coated wafers according to the steps outlined in the previous section. Depositing

Cr/Au (5 nm/50 nm in thickness) via electron beam evaporation defined a hard mask for dry etching the PVDF. Two steps of photolithography, wet etching of Cr/Au and dry etching of PVDF defined 2D patterns (28 μm in thickness) with localized regions of reduced thickness (5–13 μm in thickness). The remaining steps followed the procedures mentioned above.

Fabrication of 3D ultralow-stiffness piezoelectric mesostructures. Fabrication and transfer of 2D precursors followed the procedures for the 3D piezoelectric mesostructures described above. An additional layer of polyimide (12.5 μm in thickness) patterned by photolithography and dry etching with bonding sites defined by patterns of $\text{Al}_2\text{O}_3/\text{Ti}/\text{SiO}_2$ (50 nm/10 nm/100 nm in thickness) served as a supporting layer. After aligning this layer with the 2D precursor of PVDF on a PVA tape, the same compressive buckling steps as described previously transformed the precursor and supporting layer into a 3D geometry. Applying HCl to the bonding sites of the supporting layer dissolved the Al_2O_3 , thereby releasing this layer from the silicone elastomer to yield 3D PVDF mesostructures with ultralow stiffnesses.

Fabrication of vibration-based energy harvesters. Fabrication began with deposition of Cr/Au/Ti (10 nm/100 nm/20 nm in thickness) on one side of a film of PVDF (9 μm in thickness), and Cr/Au (10 nm/100 nm in thickness) on the other side. Laminating the PVDF onto a PDMS-coated wafer with the Cr/Au/Ti side facing up allowed for further steps in photolithography, wet etching of Cr/Au/Ti, and dry etching of PVDF to define the 2D precursors. Sonication separated the exposed Cr/Au at the bottom side from the metal patterns at the top side, thereby preventing short circuits between the top and bottom metal layers. After retrieving the 2D precursors with PVA tape, electron beam evaporation of Ti/SiO₂ (10 nm/100 nm in thickness) through a shadow mask defined the bonding sites. Aligning a supporting layer, with $\text{Al}_2\text{O}_3/\text{Ti}/\text{SiO}_2$ (50 nm/10 nm/100 nm in thickness) at the bonding sites, onto the same PVA tape completed the fabrication and transfer of the 2D precursors. The remaining compressive buckling steps followed the same procedures for fabrication of 3D ultralow-stiffness mesostructures in PVDF.

Fabrication of impact-based energy harvester and sensor. Fabrication of impact-based energy harvesters followed the procedures outlined for fabrication of vibration-based energy harvesters. Subsequent steps included drop casting and curing of silicone elastomer (Ecoflex 0050, Smooth-On) around the 3D mesostructures, and patterning silicone elastomer by use of a CO₂ laser cutting system (Universal Laser Systems).

Fabrication of 3D energy harvesters with supporting layers. Fabrication of 3D energy harvesters with supporting layers followed the steps outlined for fabrication of vibration-based energy harvesters. Subsequent conformal deposition of parylene-C (10 μm in thickness) on the harvester and dry etching of parylene-C at the top side of the structure completed the process.

Fabrication of 3D energy harvesters with patterned electrodes. Fabrication of 3D energy harvesters with patterned electrodes began with preparation of 2D precursors in PVDF as described in the fabrication of 3D piezoelectric mesostructures. Additional steps involved deposition of Cr/Au (10 nm/100 nm in thickness) on both sides of the 2D precursors through shadow masks. The transfer and buckling steps followed the procedures mentioned above.

Fabrication of 3D piezoelectric microsystems for biomedical implants. Fabrication of 3D piezoelectric microsystems for biomedical implants followed the procedures for fabrication of vibration-based energy harvesters. Subsequent steps included conformal deposition of parylene-C (2 μm in thickness) onto the 3D mesostructures.

Measurement of vibration-based energy harvesters. The data acquisition system included a vibration generator (U56001, 3B Scientific), a function generator (FG100, 3B Scientific), a vibration meter (AR63B, Smart Sensor) and a PowerLab computer interface (Model 8/35, ADInstruments). The vibration generator powered by the function generator produced periodic harmonic vibrations at programmable frequencies between 5 Hz and 800 Hz, at an acceleration of 4g. The vibration meter provided a means to calibrate the accelerations at different frequencies before testing the energy harvesters. The PowerLab system allowed recordings of output voltage through a 1 M Ω probe at a sampling rate of 200,000 samples s⁻¹. A notch filter at 60 Hz attenuated noise from the electrical lines.

Measurement of impact-based energy harvesters and sensors. The data acquisition hardware included a PowerLab system, a high-precision linear stage (ATS100-150; Aerotech, Inc.) with a LabVIEW control interface, a load cell (FC2231, TE Connectivity), an impedance analyser (Keysight E4990A) and a semiconductor parameter analyser (Agilent, 4155C). The linear stage produced periodic linear motions to press, stretch or bend the impact-based energy harvesters. The pressing tests used the load cell to measure the magnitude of the applied force. In the stretching tests, motions of the linear stage yielded different

strains applied to the impact-based energy harvester. In the bending tests, the impact-based energy harvester was attached to a PI film (75 μm in thickness), such that displacements changed its radius of curvature. The PowerLab system recorded the output voltage during pressing, stretching and bending tests via measurements through a 100 M Ω probe with a low-pass filter (30 Hz, to attenuate noise signal at high frequencies) at a sampling rate of 200,000 samples s⁻¹. The impedance analyser determined the magnitude of the impedance at frequencies between 20 Hz and 100 kHz. The semiconductor parameter analyser measured the current–voltage responses over a range of voltages from 0 to 50 V.

Cell seeding and assessment of cell viability. PVDF (9 μm in thickness) and parylene-C (4 μm in thickness) films were cut into small pieces (5.4 mm in diameter) and placed into a 96-well TCP plate. The plate was then sterilized using ethylene oxide (EtO) gas. L929 fibroblasts (passage number: 5) were seeded onto TCP, PVDF and parylene-C surfaces at a density of 10,000 cells cm⁻². Cell viability at days 1, 3 and 7 was tested with alamarBlue assay. Briefly, cells were incubated with 100 μl Dulbecco's Modified Eagle Medium (DMEM) culture medium supplemented with 10% alamarBlue solution in a cell culture incubator for 3 h. Then, the type medium was transferred into a new 96-well plate. The fluorescence intensity at 590 nm was read to evaluate cell viability. The viability data of the cells cultured on PVDF and parylene-C films were normalized based on the control cells, which were cultured on TCP. Cell viability was assessed by a live/dead kit (Invitrogen). Live/dead staining were performed at day 3 to confirm the influence of PVDF and parylene-C on cell viability. Cells were incubated with serum-free medium supplemented with 4 μM calcein AM and 2 μM ethidium homodimer-1 in a cell culture incubator for 30 min. To assess the cell attachment and spreading, cells were fixed using 4% paraformaldehyde followed by permeabilization using 0.2% triton X-100 at day 7. Then, the cells were blocked with 1% Bovine Serum Albumin (BSA) solution and stained with Alexa Fluor 488 Phalloidin and DAPI to check the cell morphology on PVDF and parylene-C films.

Evaluation of 3D piezoelectric device in animal models. All procedures associated with animal studies followed recommendations in the Guide for the Care and Use of Laboratory Animals of the National Institutes of Health. The Institutional Animal Care and Use Committee (IACUC) at Northwestern University (Protocol No. IS00005877) approved the protocol. Female mice (CD1, age at initiation of the treatment: at least 6 weeks, but not more than 15 weeks, purchased from Charles River Laboratories) were acclimated up to 5 days before surgery. Animals were anaesthetized using isoflurane gas during the implantation surgery and measurement. Fur removal and surgical exposure enabled the insertion of a 3D energy harvester into the subcutaneous region near the right flank. Bioabsorbable suturing and gluing closed the surgically exposed region with two biocompatible wires probing externally for signal readout (Supplementary Fig. 46). A PowerLab system enabled collection of the data through a 1 M Ω probe with a bandpass filter (0.1–30 Hz, to attenuate noise signals at high frequencies and avoid a pyroelectric signal from temperature fluctuations) at a sampling rate of 200,000 samples s⁻¹.

Reporting Summary. Further information on experimental design is available in the Nature Research Reporting Summary linked to this article.

Data availability

The data that support the plots within this paper and other findings of this study are available from the corresponding author upon reasonable request.

Received: 7 August 2018; Accepted: 6 December 2018;
Published online: 16 January 2019

References

- Kim, D. H. et al. Epidermal electronics. *Science* **333**, 838–843 (2011).
- Larson, C. et al. Highly stretchable electroluminescent skin for optical signaling and tactile sensing. *Science* **351**, 1071–1074 (2016).
- Tian, B. et al. Macroporous nanowire nanoelectronic scaffolds for synthetic tissues. *Nat. Mater.* **11**, 986–994 (2012).
- Hwang, G. T. et al. Self-powered cardiac pacemaker enabled by flexible single crystalline PMN-PT piezoelectric energy harvester. *Adv. Mater.* **26**, 4880–4887 (2014).
- Fan, F. R., Tian, Z. Q. & Lin Wang, Z. Flexible triboelectric generator. *Nano Energy* **1**, 328–334 (2012).
- Yin, J. et al. Generating electricity by moving a droplet of ionic liquid along graphene. *Nat. Nanotech.* **9**, 378–383 (2014).
- Jinno, H. et al. Stretchable and waterproof elastomer-coated organic photovoltaics for washable electronic textile applications. *Nat. Energy* **2**, 780–785 (2017).
- Zhao, J. et al. Air-stable and freestanding lithium alloy/graphene foil as an alternative to lithium metal anodes. *Nat. Nanotech.* **12**, 993–999 (2017).

9. Li, M., Tang, H. X. & Roukes, M. L. Ultra-sensitive NEMS-based cantilevers for sensing, scanned probe and very high-frequency applications. *Nat. Nanotech.* **2**, 114–120 (2007).
10. Kan, T. et al. Enantiomeric switching of chiral metamaterial for terahertz polarization modulation employing vertically deformable MEMS spirals. *Nat. Commun.* **6**, 8422 (2015).
11. Nguyen, T. D. et al. Piezoelectric nanoribbons for monitoring cellular deformations. *Nat. Nanotech.* **7**, 587–593 (2012).
12. Wu, W., Wen, X. & Wang, Z. L. Taxel-addressable matrix of vertical-nanowire piezotronic transistors for active and adaptive tactile imaging. *Science* **340**, 952–957 (2013).
13. Yu, X. et al. Needle-shaped ultrathin piezoelectric microsystem for guided tissue targeting via mechanical sensing. *Nat. Biomed. Eng.* **2**, 162–172 (2018).
14. Yang, J. M. et al. Simultaneous functional photoacoustic and ultrasonic endoscopy of internal organs in vivo. *Nat. Med.* **18**, 1297–1302 (2012).
15. Hu, H. et al. Stretchable ultrasonic transducer arrays for three-dimensional imaging on complex surfaces. *Sci. Adv.* **4**, eaar3979 (2018).
16. Wang, X., Song, J., Liu, J. & Zhong, L. W. Direct-current nanogenerator driven by ultrasonic waves. *Science* **316**, 102–105 (2007).
17. Dagdeviren, C. et al. Conformal piezoelectric energy harvesting and storage from motions of the heart, lung, and diaphragm. *Proc. Natl Acad. Sci. USA* **111**, 1927–1932 (2014).
18. Baek, S. H. et al. Giant piezoelectricity on Si for hyperactive MEMS. *Science* **334**, 958–961 (2011).
19. Ma, K. Y., Chirarattananon, P., Fuller, S. B. & Wood, R. J. Controlled flight of a biologically inspired, insect-scale robot. *Science* **340**, 603–607 (2013).
20. You, Y. M. et al. An organic-inorganic perovskite ferroelectric with large piezoelectric response. *Science* **357**, 306–309 (2017).
21. Curry, E. J. et al. Biodegradable piezoelectric force sensor. *Proc. Natl Acad. Sci. USA* **115**, 909–914 (2018).
22. Wu, W. et al. Piezoelectricity of single-atomic-layer MoS₂ for energy conversion and piezotronics. *Nature* **514**, 470–474 (2014).
23. Zhu, H. et al. Observation of piezoelectricity in free-standing monolayer MoS₂. *Nat. Nanotech.* **10**, 151–155 (2015).
24. Lee, B. Y. et al. Virus-based piezoelectric energy generation. *Nat. Nanotech.* **7**, 351–356 (2012).
25. Chen, X., Mahadevan, L., Driks, A. & Sahin, O. Bacillus spores as building blocks for stimuli-responsive materials and nanogenerators. *Nat. Nanotech.* **9**, 137–141 (2014).
26. Li, M. et al. Revisiting the δ -phase of poly(vinylidene fluoride) for solution-processed ferroelectric thin films. *Nat. Mater.* **12**, 433–438 (2013).
27. Li, F. et al. Ultrahigh piezoelectricity in ferroelectric ceramics by design. *Nat. Mater.* **17**, 349–354 (2018).
28. Yan, Y., Zhou, J. E., Maurya, D., Wang, Y. U. & Priya, S. Giant piezoelectric voltage coefficient in grain-oriented modified PbTiO₃ material. *Nat. Commun.* **7**, 13089 (2016).
29. Qin, Y., Wang, X. & Wang, Z. L. Microfibre-nanowire hybrid structure for energy scavenging. *Nature* **451**, 809–813 (2008).
30. Qi, Y. et al. Enhanced piezoelectricity and stretchability in energy harvesting devices fabricated from buckled PZT ribbons. *Nano. Lett.* **11**, 1331–1336 (2011).
31. Han, M. et al. r-shaped hybrid nanogenerator with enhanced piezoelectricity. *ACS Nano* **7**, 8554–8560 (2013).
32. Saadon, S. & Sidek, O. A review of vibration-based MEMS piezoelectric energy harvesters. *Energy Convers. Manag.* **52**, 500–504 (2011).
33. Meza, L. R., Das, S. & Greer, J. R. Strong, lightweight, and recoverable three-dimensional ceramic nanolattices. *Science* **345**, 1322–1326 (2014).
34. Cavallo, F. & Lagally, M. G. Nano-origami: Art and function. *Nano Today* **10**, 538–541 (2015).
35. Sydney Gladman, A., Matsumoto, E. A., Nuzzo, R. G., Mahadevan, L. & Lewis, J. A. Biomimetic 4D printing. *Nat. Mater.* **15**, 413–418 (2016).
36. Xu, S. et al. Assembly of micro/nanomaterials into complex, three-dimensional architectures by compressive buckling. *Science* **347**, 154–159 (2015).
37. Yan, Z. et al. Mechanical assembly of complex, 3D mesostructures from releasable multilayers of advanced materials. *Sci. Adv.* **2**, e1601014 (2016).
38. Yan, Z. et al. Deterministic assembly of 3D mesostructures in advanced materials via compressive buckling: A short review of recent progress. *Extrem. Mech. Lett.* **11**, 96–104 (2017).
39. Fu, H. et al. Morphable 3D mesostructures and microelectronic devices by multistable buckling mechanics. *Nat. Mater.* **17**, 268–276 (2018).
40. Lee, W. et al. Two-dimensional materials in functional three-dimensional architectures with applications in photodetection and imaging. *Nat. Commun.* **9**, 1417 (2018).
41. Zhang, Y. et al. Printing, folding and assembly methods for forming 3D mesostructures in advanced materials. *Nat. Rev. Mater.* **2**, 17019 (2017).
42. Wang, S. et al. Mechanics of curvilinear electronics. *Soft Matter* **6**, 5757–5763 (2010).
43. Persson, B. N. J., Albohr, O., Tartaglino, U., Volokitin, A. I. & Tosatti, E. On the nature of surface roughness with application to contact mechanics, sealing, rubber friction and adhesion. *J. Phys. Condens. Matter* **17**, 1–62 (2005).
44. Yin, S. et al. Measuring single cardiac myocyte contractile force via moving a magnetic bead. *Biophys. J.* **88**, 1489–1495 (2005).
45. Raman, R. et al. Optogenetic skeletal muscle-powered adaptive biological machines. *Proc. Natl Acad. Sci. USA* **113**, 3497–3502 (2016).
46. Ning, X. et al. 3D tunable, multiscale, and multistable vibrational micro-platforms assembled by compressive buckling. *Adv. Funct. Mater.* **27**, 1605914 (2017).
47. Kulah, H. & Najafi, K. Energy scavenging from low-frequency vibrations by using frequency up-conversion for wireless sensor applications. *IEEE Sens. J.* **8**, 261–268 (2008).
48. Zi, Y. et al. Harvesting low-frequency (< 5 Hz) irregular mechanical energy: A possible killer application of triboelectric nanogenerator. *ACS Nano* **10**, 4797–4805 (2016).
49. Humood, M. et al. Fabrication and deformation of 3D multilayered kirigami microstructures. *Small* **14**, 1703852 (2018).
50. Ranzani, T., Gerboni, G., Cianchetti, M. & Menciassi, A. A bioinspired soft manipulator for minimally invasive surgery. *Bioinspir. Biomim.* **10**, 035008 (2015).

Acknowledgements

J.A.R. acknowledges support from the US Department of Energy, Office of Science, Basic Energy Sciences (DE-FG02-07ER46471). Y.Z. acknowledges support from the National Natural Science Foundation of China (11722217) and the Tsinghua National Laboratory for Information Science and Technology. Y.H. acknowledges support from the NSF (CMMI1400169, CMMI1534120 and CMMI1635443). Y.X. acknowledges support from the Ryan Fellowship and the Northwestern University International Institute for Nanotechnology.

Author contributions

M.H., H.W., Z.Y., Y.Z., Y.H. and J.A.R. conceived the idea and designed the research. M.H., Y.Y., C.L., Z.Y. and J.L. performed micro-fabrication of all structures and devices. M.H., C.L., W.B. and H.Z. performed measurements and analysed the experimental data. M.H., W.B. and I.K. evaluated the devices in animal models. X.W. and B.A. performed cell seeding and cell viability assay under the supervision of G.A.A. H.W., Y.Z. and Y.H. led the mechanical modelling and theoretical studies, with assistance from H. Li. Y.X. and H. Luan. M.H., H.W., Y.Z., Y.H. and J.A.R. wrote the manuscript.

Competing interests

The authors declare no competing interests.

Additional information

Supplementary information is available for this paper at <https://doi.org/10.1038/s41928-018-0189-7>.

Reprints and permissions information is available at www.nature.com/reprints.

Correspondence and requests for materials should be addressed to Y.Z. or Y.H. or J.A.R.

Publisher's note: Springer Nature remains neutral with regard to jurisdictional claims in published maps and institutional affiliations.

© The Author(s), under exclusive licence to Springer Nature Limited 2019

Reporting Summary

Nature Research wishes to improve the reproducibility of the work that we publish. This form provides structure for consistency and transparency in reporting. For further information on Nature Research policies, see [Authors & Referees](#) and the [Editorial Policy Checklist](#).

Statistical parameters

When statistical analyses are reported, confirm that the following items are present in the relevant location (e.g. figure legend, table legend, main text, or Methods section).

n/a | Confirmed

- The exact sample size (n) for each experimental group/condition, given as a discrete number and unit of measurement
- An indication of whether measurements were taken from distinct samples or whether the same sample was measured repeatedly
- The statistical test(s) used AND whether they are one- or two-sided
Only common tests should be described solely by name; describe more complex techniques in the Methods section.
- A description of all covariates tested
- A description of any assumptions or corrections, such as tests of normality and adjustment for multiple comparisons
- A full description of the statistics including central tendency (e.g. means) or other basic estimates (e.g. regression coefficient) AND variation (e.g. standard deviation) or associated estimates of uncertainty (e.g. confidence intervals)
- For null hypothesis testing, the test statistic (e.g. F , t , r) with confidence intervals, effect sizes, degrees of freedom and P value noted
Give P values as exact values whenever suitable.
- For Bayesian analysis, information on the choice of priors and Markov chain Monte Carlo settings
- For hierarchical and complex designs, identification of the appropriate level for tests and full reporting of outcomes
- Estimates of effect sizes (e.g. Cohen's d , Pearson's r), indicating how they were calculated
- Clearly defined error bars
State explicitly what error bars represent (e.g. SD, SE, CI)

Our web collection on [statistics for biologists](#) may be useful.

Software and code

Policy information about [availability of computer code](#)

Data collection

Data analysis

For manuscripts utilizing custom algorithms or software that are central to the research but not yet described in published literature, software must be made available to editors/reviewers upon request. We strongly encourage code deposition in a community repository (e.g. GitHub). See the Nature Research [guidelines for submitting code & software](#) for further information.

Data

Policy information about [availability of data](#)

All manuscripts must include a [data availability statement](#). This statement should provide the following information, where applicable:

- Accession codes, unique identifiers, or web links for publicly available datasets
- A list of figures that have associated raw data
- A description of any restrictions on data availability

Field-specific reporting

Please select the best fit for your research. If you are not sure, read the appropriate sections before making your selection.

Life sciences Behavioural & social sciences Ecological, evolutionary & environmental sciences

For a reference copy of the document with all sections, see [nature.com/authors/policies/ReportingSummary-flat.pdf](https://www.nature.com/authors/policies/ReportingSummary-flat.pdf)

Life sciences study design

All studies must disclose on these points even when the disclosure is negative.

Sample size	Sample size was n=3 mice for the measurements of 3D devices. Output signals of the 3D and 2D devices were measured three times after implantation. Duration of each measurement ranges from 1 min to 5 min. Over twenty similar mouse behaviors appeared in the measurements. Three 3D devices were implanted.
Data exclusions	No data were excluded from the analyses.
Replication	Data measured from the implanted 3D and 2D devices were reproducible. Similar output of the device appeared in three different measurements which include over twenty mouse behaviors.
Randomization	All devices and animals tested were selected randomly.
Blinding	The investigators were blinded to group allocation during data collection and analysis (i.e., the assessment of cell viability and comparison of the output voltage of implanted 3D and 2D devices).

Reporting for specific materials, systems and methods

Materials & experimental systems

n/a	Involvement
<input checked="" type="checkbox"/>	<input type="checkbox"/> Unique biological materials
<input checked="" type="checkbox"/>	<input type="checkbox"/> Antibodies
<input checked="" type="checkbox"/>	<input type="checkbox"/> Eukaryotic cell lines
<input checked="" type="checkbox"/>	<input type="checkbox"/> Palaeontology
<input type="checkbox"/>	<input checked="" type="checkbox"/> Animals and other organisms
<input checked="" type="checkbox"/>	<input type="checkbox"/> Human research participants

Methods

n/a	Involvement
<input checked="" type="checkbox"/>	<input type="checkbox"/> ChIP-seq
<input checked="" type="checkbox"/>	<input type="checkbox"/> Flow cytometry
<input checked="" type="checkbox"/>	<input type="checkbox"/> MRI-based neuroimaging

Animals and other organisms

Policy information about [studies involving animals](#); [ARRIVE guidelines](#) recommended for reporting animal research

Laboratory animals	Species: Mice. Strain: CD1, Charles River, CrI:CD1(ICR). Sex: female. Age at initiation of the treatment: At least 6 weeks, but not more than 15 weeks.
Wild animals	N/A
Field-collected samples	N/A

In the format provided by the authors and unedited.

Three-dimensional piezoelectric polymer microsystems for vibrational energy harvesting, robotic interfaces and biomedical implants

Mengdi Han^{1,14}, Heling Wang^{1,2,3,4,14}, Yiyuan Yang³, Cunman Liang^{1,5}, Wubin Bai^{1,2}, Zheng Yan⁶, Haibo Li^{4,7}, Yeguang Xue^{2,3,4}, Xinlong Wang⁸, Banu Akar⁸, Hangbo Zhao¹, Haiwen Luan^{2,3,4}, Jaeman Lim¹, Irawati Kandela⁹, Guillermo A. Ameer^{8,10,11}, Yihui Zhang^{12*}, Yonggang Huang^{1,2,3,4*} and John A. Rogers^{1,2,3,8,11,13*}

¹Center for Bio-Integrated Electronics, Northwestern University, Evanston, IL, USA. ²Department of Materials Science and Engineering, Northwestern University, Evanston, IL, USA. ³Department of Mechanical Engineering, Northwestern University, Evanston, IL, USA. ⁴Departments of Civil and Environmental Engineering, Northwestern University, Evanston, IL, USA. ⁵Key Laboratory of Mechanism Theory and Equipment Design of Ministry of Education, School of Mechanical Engineering, Tianjin University, Tianjin, China. ⁶Departments of Biomedical, Biological & Chemical Engineering, Mechanical and Aerospace Engineering, University of Missouri, Columbia, MO, USA. ⁷School of Naval Architecture, Ocean and Civil Engineering (State Key Laboratory of Ocean Engineering), Shanghai Jiaotong University, Shanghai, China. ⁸Department of Biomedical Engineering, Northwestern University, Evanston, IL, USA. ⁹The Center for Developmental Therapeutics, Northwestern University, Evanston, IL, USA. ¹⁰Department of Surgery at Northwestern University Feinberg School of Medicine, Chicago, IL, USA. ¹¹Center for Advanced Regenerative Engineering, Northwestern University, Evanston, IL, USA. ¹²Center for Flexible Electronics Technology and Center for Mechanics and Materials; AML, Department of Engineering Mechanics, Tsinghua University, Beijing, China. ¹³Departments of Neurological Surgery, Chemistry, Electrical Engineering and Computer Science; and Simpson Querrey Institute for BioNanotechnology, Northwestern University, Evanston, IL, USA. ¹⁴These authors contributed equally: Mengdi Han, Heling Wang. *e-mail: yihuzhang@tsinghua.edu.cn; y-huang@northwestern.edu; jrogers@northwestern.edu

Supplementary Note 1: Representative step-by-step fabrication procedures for 3D piezoelectric microsystems

Preparing substrates

1. Clean PVDF film (28 μm in thickness) with IPA
2. Deposit Cr/Au (5 nm/50 nm in thickness) on both sides of PVDF film
3. Clean silicon wafer (500 μm in thickness) with acetone and IPA
4. Spin coat PDMS (1:10) at 3000 rpm on silicon wafer
5. Bake at 70 °C for 1 h
6. Transfer PVDF film onto PDMS-coated silicon wafer

Defining 2D patterns

7. Define 2D pattern with photoresist (AZ 5214)
8. Wet etch Au and Cr with commercial etchants
9. Dry etch PVDF through RIE (220 mTorr, 25 sccm O₂, RF power of 200 W for 120 min)

Defining creases

10. Define creases with photoresist (AZ 5214)
11. Wet etch Au and Cr with commercial etchants
12. Dry etch PVDF through RIE (220 mTorr, 25 sccm O₂, RF power of 200 W for 90 min). Controlling the etching time yields creases with different thicknesses.

Defining top electrode

13. Define top electrode with photoresist (AZ 4620)
14. Wet etch Au and Cr with commercial etchants

Defining bottom electrode

15. Transfer PVDF film to PVA tape
16. Laminate PVA tape onto another PDMS-coated silicon wafer, with PVDF side facing up

17. Clamp the sample and dissolve PVA tape with warm water

18. Define bottom electrode with photoresist (AZ 4620)

19. Wet etch Au and Cr with commercial etchants

Transfer printing

20. Transfer PVDF film to PVA tape

21. Laminate PVA tape onto another PDMS-coated silicon wafer, with PVDF side facing up

22. Clamp the sample and dissolve PVA tape with warm water

23. Transfer PVDF film to PVA tape again (to flip the top and bottom sides)

24. Deposit Ti/SiO₂ (10 nm/100 nm in thickness) through shadow mask to define the bonding sites

Compressive buckling

25. UVO treatment of silicone elastomer (Dragon Skin, 700 μm in thickness) and PVDF 2D precursors for 5 min

26. Transfer print PVDF 2D precursors onto stretched silicone elastomer

27. Heat the samples in the oven at 70 °C for 10 min

28. Dissolve PVA tape with warm water

29. Release stretched silicone elastomer to form 3D PVDF mesostructures

Supplementary Note 2: Finite element analysis (FEA) and calculation of output voltage

Shape, deformation and vibration of 3D structures

FEA was adopted to predict the 2D-to-3D shape transformation induced by the compressive strain, the deformation of the 3D structure under applied force and the vibration driven by a vibrational platform. FEA was conducted by the commercial software ABAQUS (version 6.14, standard). To overcome the energy barrier that prevented the 2D-to-3D shape transformation, an initial geometric imperfection was introduced such that the 2D precursor evolved to the accurate 3D shape under compressive strain. For those structures with ultra-low stiffness serpentine pattern, the initial geometric imperfection was introduced only into the temporary supporting layer that assisted the buckling via contact. Eight-node solid element modeled the

underlying elastomeric substrate (D-skin), with the Mooney-Rivlin constitutive relationship. Eight-node solid element also modeled the added copper mass (Cu) with the linear elastic constitutive relationship. Four-node finite-strain shell element modeled the precursor, with the linear elastic constitutive relationship. The precursor consisted of piezoelectric material PVDF, metal electrodes (Au, Cr and Ti) and supporting layer (PI). The material properties (Young's modulus E , Poisson's ratio ν and density ρ) are $E_{\text{Substrate}}=166$ kPa, $\nu_{\text{Substrate}}=0.49$, $\rho_{\text{Substrate}}=1070$ kg/m³, $E_{\text{Cu}}=128$ kPa, $\nu_{\text{Cu}}=0.36$, $\rho_{\text{Cu}}=8960$ kg/m³, $E_{\text{PVDF}}=2$ GPa, $\nu_{\text{PVDF}}=0.39$, $\rho_{\text{PVDF}}=1800$ kg/m³, $E_{\text{Au}}=78$ GPa, $\nu_{\text{Au}}=0.44$, $\rho_{\text{Au}}=19320$ kg/m³, $E_{\text{Cr}}=279$ GP, $\nu_{\text{Cr}}=0.21$, $\rho_{\text{Cr}}=7190$ kg/m³, $E_{\text{Ti}}=110$ GPa, $\nu_{\text{Ti}}=0.32$, $\rho_{\text{Ti}}=4506$ kg/m³, $E_{\text{PI}}=2.5$ GPa, $\nu_{\text{PI}}=0.34$ and $\rho_{\text{PI}}=1420$ kg/m³.

Calculation of output voltage

The open-circuit output voltage during vibration was calculated from the piezoelectric constitutive relationship and the membrane strain obtained by FEA. Assuming that the PVDF was polarized along its thickness direction (3- direction), its constitutive relationship was

$$D_3 = e_{31}\varepsilon_{11} + e_{31}\varepsilon_{22} + k_{33}E_3, \quad (\text{S1})$$

where ε_{11} and ε_{22} were the strains, E_3 was the electrical field, D_3 was the electrical displacement, $e_{31}=-0.03$ N/(V.m) was the piezoelectric constant and $k_{33}=8.85 \times 10^{-11}$ F/m was the dielectric constant. The normal strain along 3- direction was neglected. Under the open-circuit condition

$$\int_{-h_{\text{PVDF}}/2}^{h_{\text{PVDF}}/2} D_3 dz = 0, \quad (\text{S2})$$

the open-circuit output voltage at point (x, y) was

$$v_{\text{open-circuit}}(x, y) = \int_{-h_{\text{PVDF}}/2}^{h_{\text{PVDF}}/2} E_3 dz = -\frac{e_{31}h_{\text{PVDF}}}{k_{33}} \left[\varepsilon_{11(m)}(x, y) + \varepsilon_{22(m)}(x, y) \right], \quad (\text{S3})$$

where h_{PVDF} was the PVDF thickness, $\varepsilon_{11(m)}$ and $\varepsilon_{22(m)}$ were the membrane strains in PVDF obtained by FEA.

The net output voltage was the average of $v_{\text{open-circuit}}(x, y)$ over the region Ω with the electrode

$$V_{\text{open-circuit}} = \frac{1}{A_{\Omega}} \int_{\Omega} v_{\text{open-circuit}}(x, y) dx dy, \quad (\text{S4})$$

where A_{Ω} is the area of Ω . In the actual experiment condition, the voltage had to be measured in a circuit with finite resistance R . Therefore, the open-circuit condition Eq. (S2) should be replaced by [Ref. 1]

$$\frac{V}{R} = -A_{\Omega} \frac{dD_3}{dt}, \quad (S5)$$

which lead to

$$\frac{dV}{dt} + \frac{h_{\text{PVDF}}}{A_{\Omega} R k_{33}} = -\frac{e_{31} h_{\text{PVDF}}}{k_{33}} \left(\frac{d\varepsilon_{11(m)}}{dt} + \frac{d\varepsilon_{22(m)}}{dt} \right), \quad (S6)$$

where V was the output voltage. Under the initial condition that $V=0$ at $t=0$, the output voltage was

$$V = -\frac{e_{31} h_{\text{PVDF}}}{k_{33}} e^{-\frac{h_{\text{PVDF}}}{A_{\Omega} R k_{33}} t} \int_0^t \left(\frac{d\varepsilon_{11(m)}}{ds} + \frac{d\varepsilon_{22(m)}}{ds} \right) e^{\frac{h_{\text{PVDF}} s}{A_{\Omega} R k_{33}}} ds, \quad (S7)$$

Supplementary Note 3: A numerical example of the energetic analysis on buckling process

A numerical example is presented in this supplementary note to demonstrate that the serpentine pattern could not delaminate from the substrate to buckle without the temporary supporting layer but could remain in the buckle-up state after removing the supporting layer. A representative 2D precursor with serpentine pattern is shown in Supplementary Fig. 10a. Supplementary Fig. 10b and Supplementary Fig. 10c show its local buckling state and global buckling state respectively. The total energy W of the two states are compared in Supplementary Fig. 10d. The total energy consists of the strain energy and the adhesion energy $W_{\text{Adhesion}} = \gamma A_{\text{Adhesion}}$, where γ is the work of adhesion and A_{Adhesion} is the area of the serpentine pattern bonded to the substrate. γ is assumed to be 0.16 N/m [Ref. 2] in this analysis. FEA result shown in Supplementary Fig. 10d indicates that the local buckling state has a lower energy than the global buckling state. Therefore, without the supporting layer the serpentine pattern tends to adhere to the substrate. However, as shown by Supplementary Fig. 10e, the global buckling state is a local energy minimum such that the serpentine pattern can remain in this state after removing the supporting layer which assists the serpentine pattern to buckle-up.

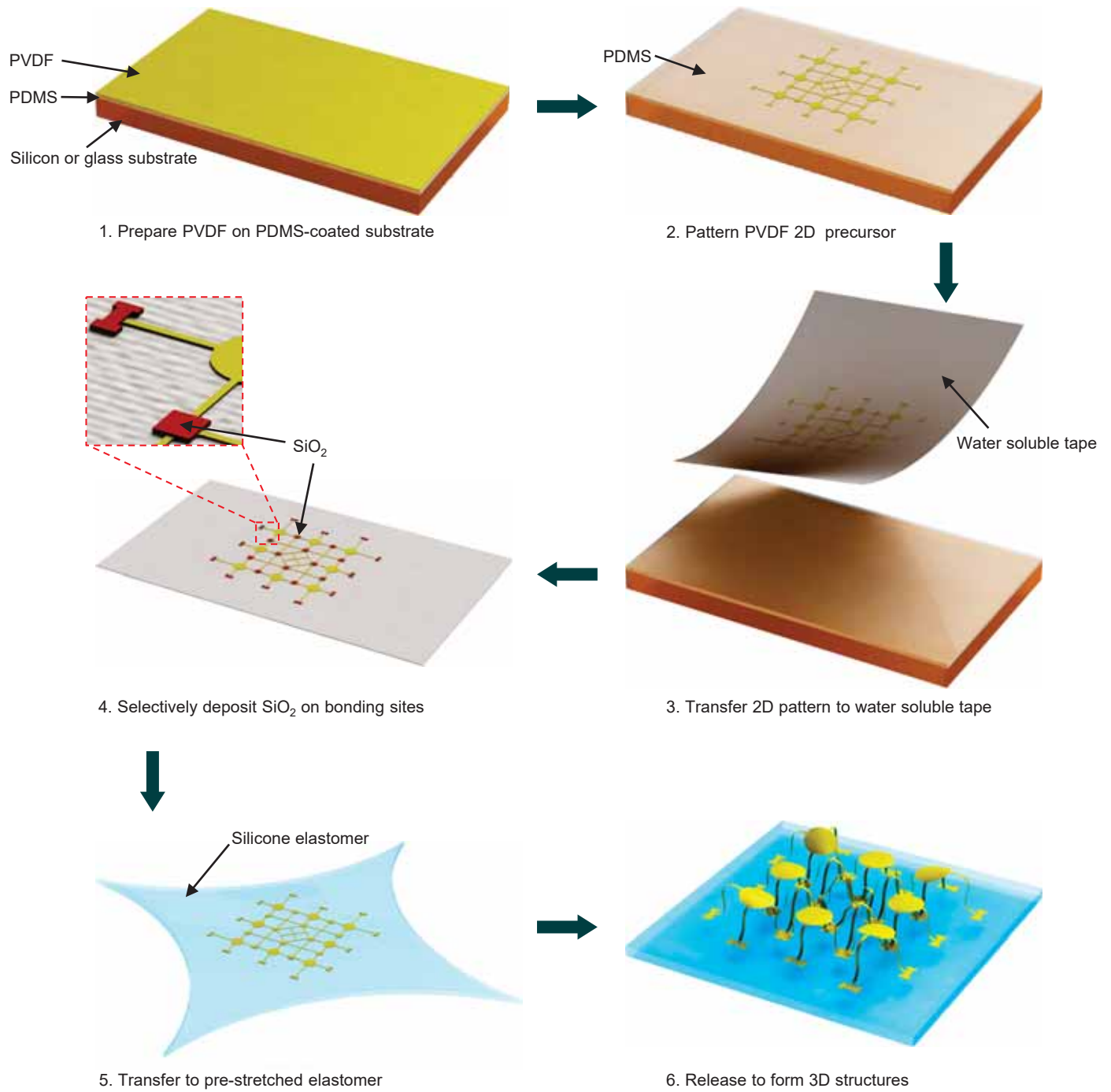
FEA results in Supplementary Fig. 11b show that the structure in Fig. 2e must overcome an energy barrier of 5.5 nJ to switch from the buckle up state to the buckle down state. Assuming that all of the serpentine ribbon attaches to the PI supporting layer, the adhesion energy is estimated as ~28 nJ (serpentine area is calculated as 0.35 mm²; the work of adhesion between PI and electrode is 0.08 J/m² [Ref. 3]). However, optical images in experiment show that only a small part of the serpentine ribbon attaches to the supporting layer when the structure buckles up (Supplementary Fig. 8a). Therefore, the adhesion energy becomes much smaller and is insufficient to overcome the energy barrier.

Supplementary Note 4: Validation of the scaling laws

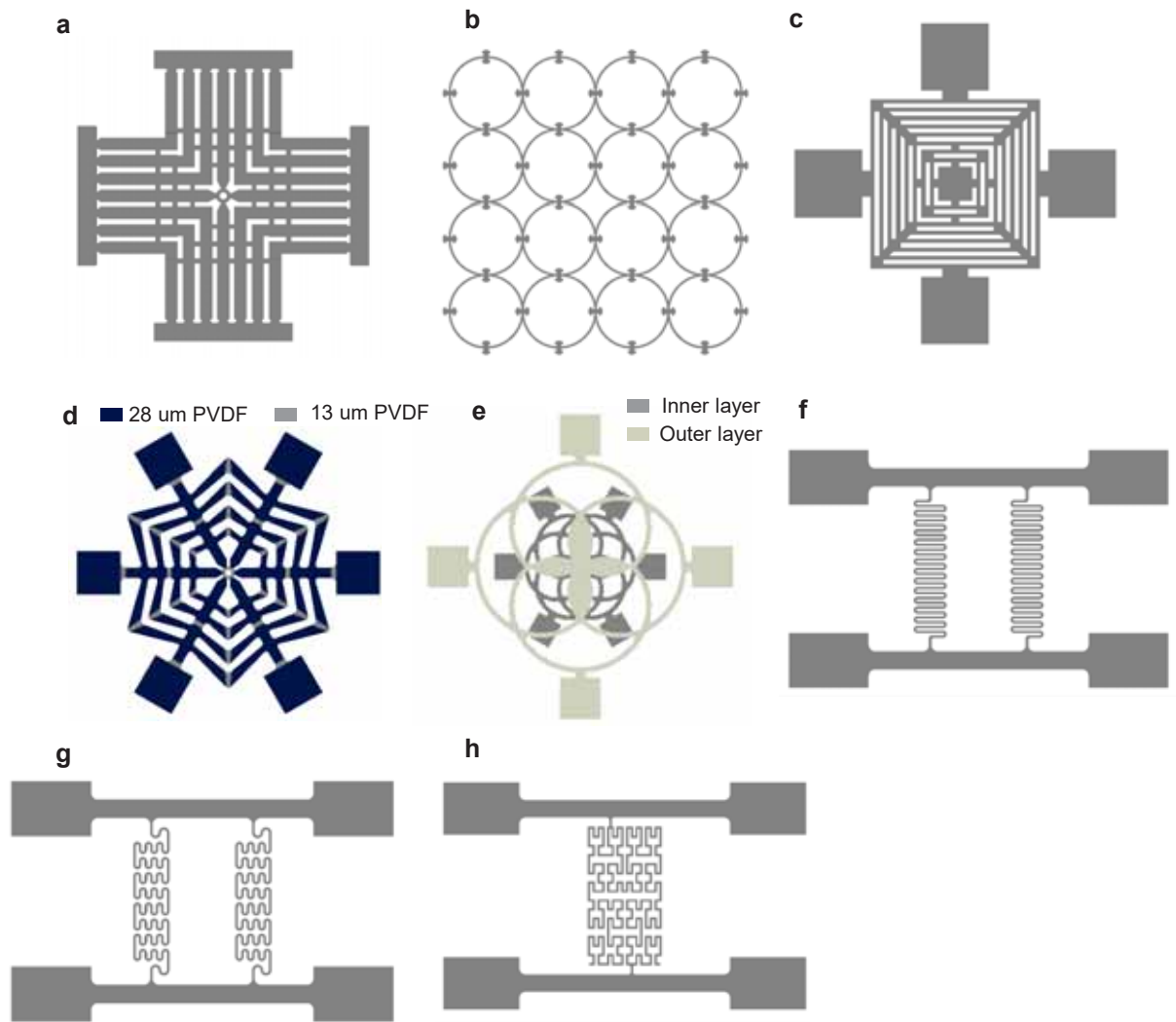
FEA Validations of the scaling laws presented in the manuscript are presented in this Supplementary note. To validate Eq. (1), FEA is conducted on the structure with serpentine pattern shown in Supplementary Fig. 28. The default geometry/material parameters are $L=2.5$ mm, $H=1.2$ mm, $S=25$ mm, $h=9$ μm , $b=50$ μm and $E=2$ GPa. One of the above parameters are changed at one time with the others fixed. FEA then obtains the displacement u vs. force F curves. After normalizing u by L and F by $\frac{Ebh^3L}{H^2S}$, the $\frac{u}{L}$ vs. $\frac{FH^2S}{Ebh^3L}$ curves are the same for various sets of parameters as shown in Supplementary Figs. 30a-f, which validates the scaling law Eq. (1). The stiffness $K = \left. \frac{\partial F}{\partial u} \right|_{u \rightarrow 0}$ is then calculated from the u vs. force F curves obtained above. As shown in Supplementary Fig. 32, the K vs. $\frac{Ebh^3}{H^2S}$ relationship falls on a straight line, which validates that K is proportional to $\frac{Ebh^3}{H^2S}$. To validate the scaling law of the resonant frequency (f) Eq. (2), with one of the three parameters (h , H , S) changed at a time, FEA prediction of the f vs. $\frac{h}{HS} \sqrt{\frac{E}{\rho}}$ relationship falls on a straight line as shown in Fig. 2l and Supplementary Fig. 33a. The coefficient α in the scaling law, i.e. the slope of the straight line in Fig. 2l, is fitted to be 0.65 by the method of least squares. The scaling law also suggests that the resonant frequency does not depend on the serpentine length L and ribbon width w . FEA results presented in Supplementary Figs. 33b and c show that the resonant frequency f changes little with L and w , which is consistent with the scaling law.

Reference:

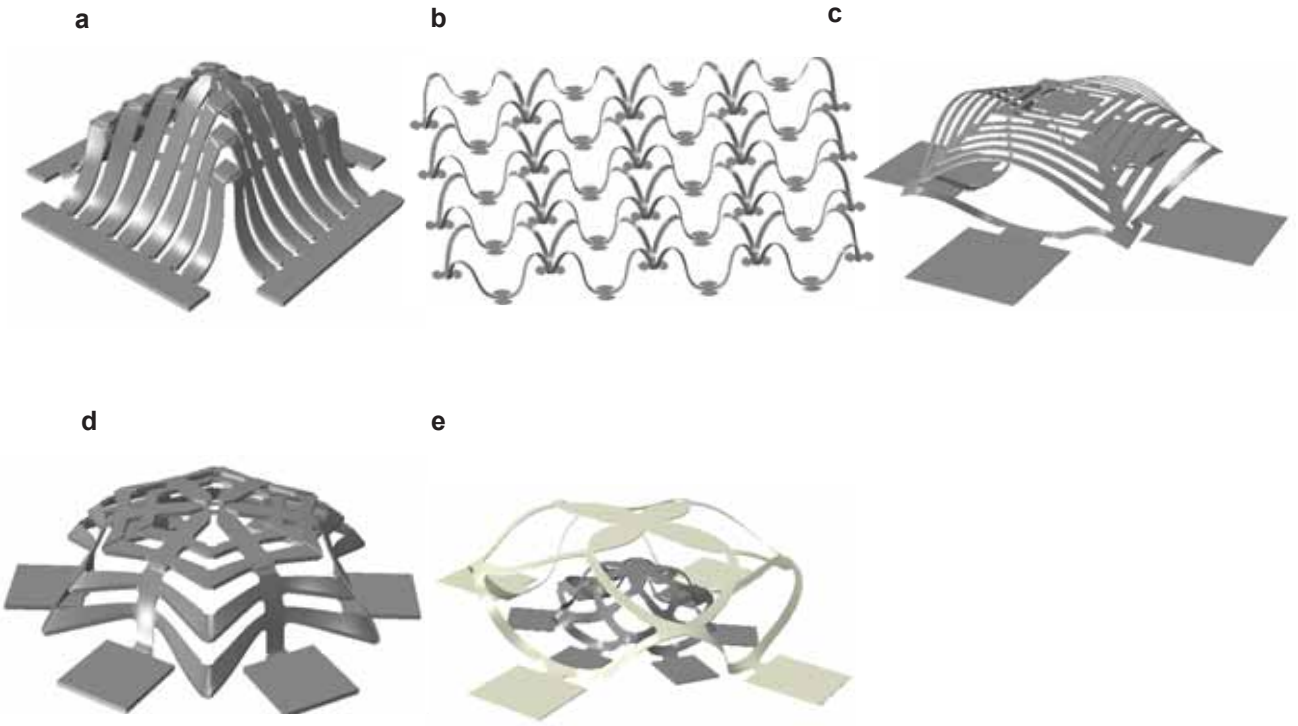
1. Su, Y., Dagdeviren, C. & Li, R. Measured output voltages of piezoelectric devices depend on the resistance of voltmeter. *Advanced Functional Materials* **25**, 5320–5325 (2015).
2. Wang, S. et al. Mechanics of curvilinear electronics. *Soft Matter* **6**, 5757–5763 (2010).
3. Park, S. et al. Influence of surface treatment of polyimide film on adhesion enhancement between polyimide and metal films. *Bulletin of the Korean Chemical Society* **28**, 188–192 (2007).



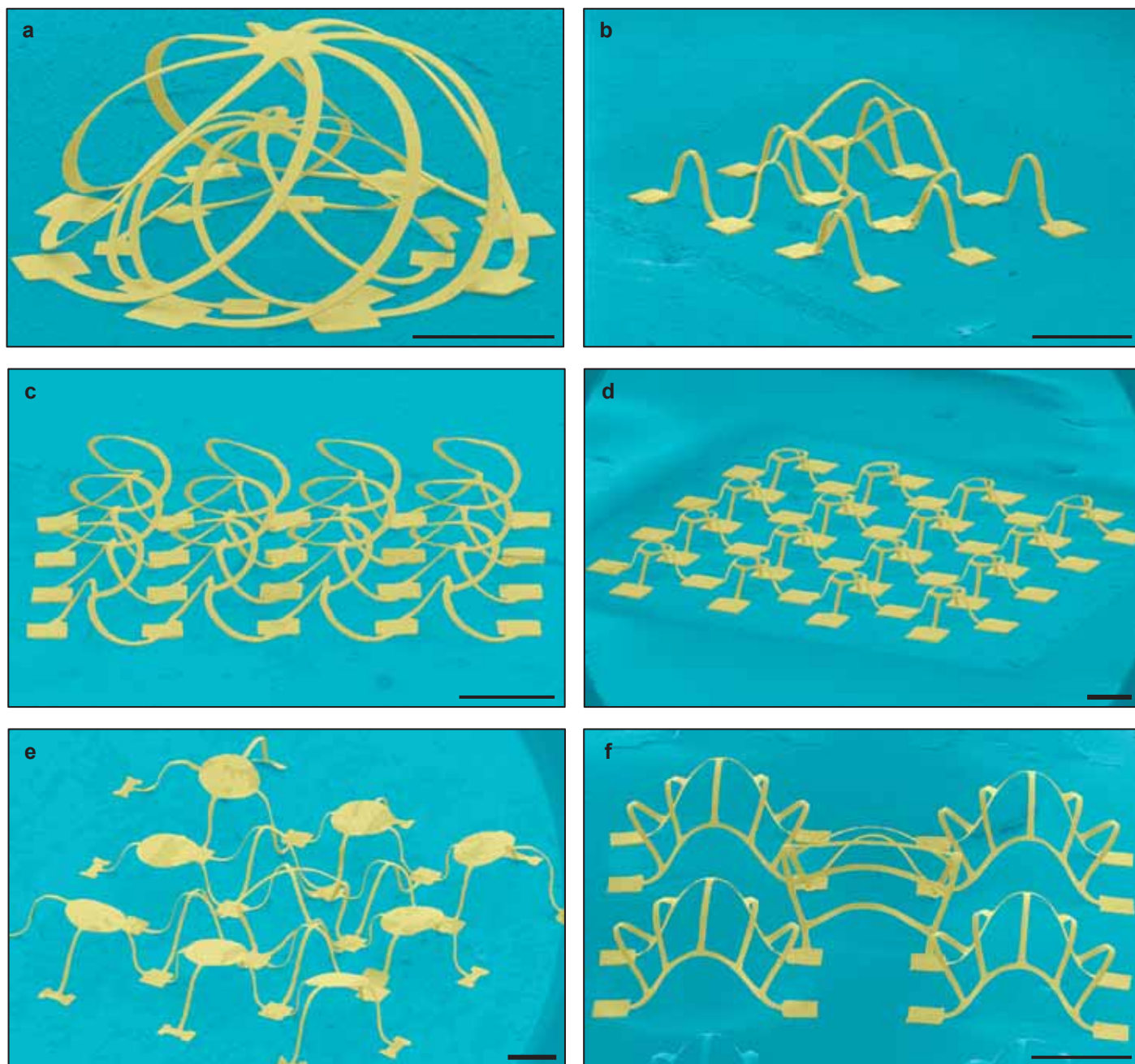
Supplementary Figure 1. Fabrication scheme for 3D piezoelectric microsystems



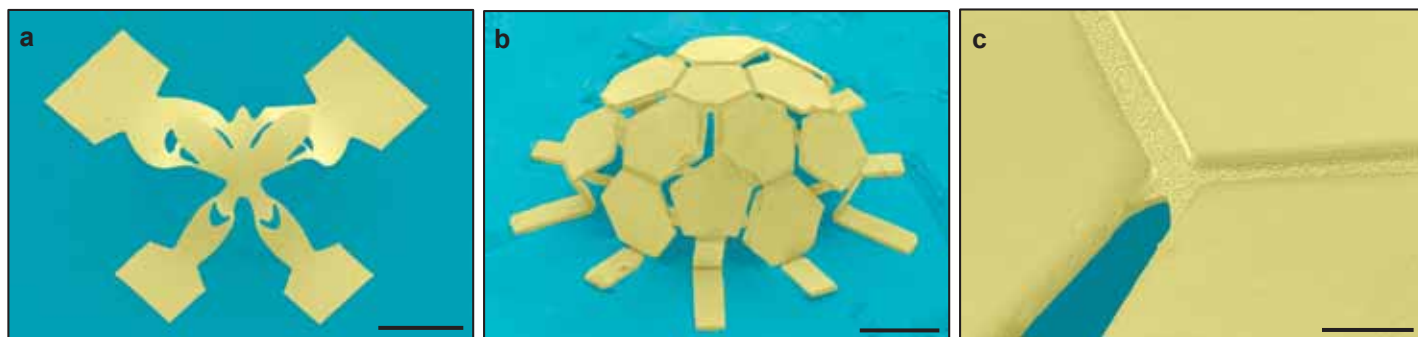
Supplementary Figure 2. Precursor of the structures shown in Fig.1.



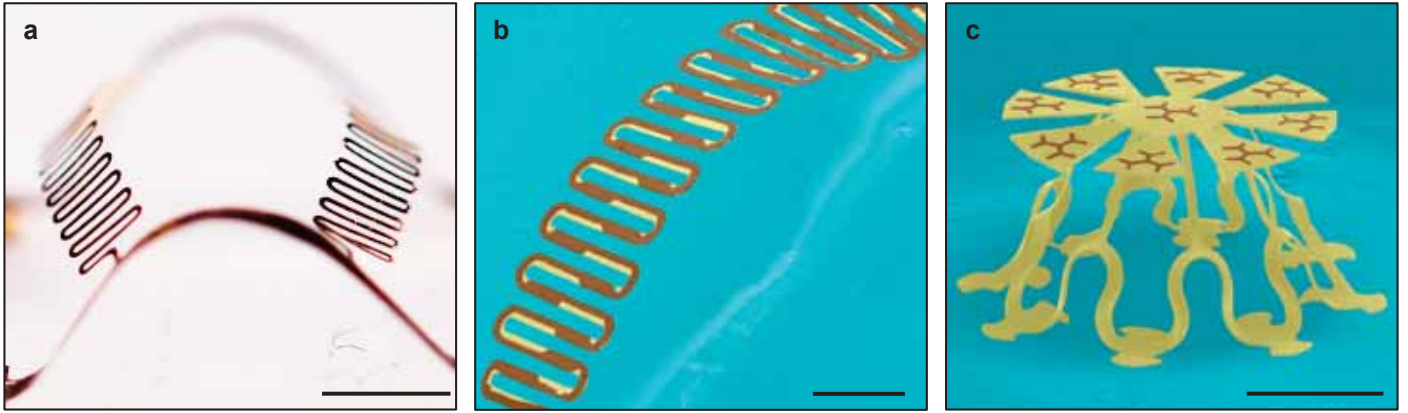
Supplementary Figure 3. FEA prediction of the buckled shape for the structures in Fig. 1a and b.



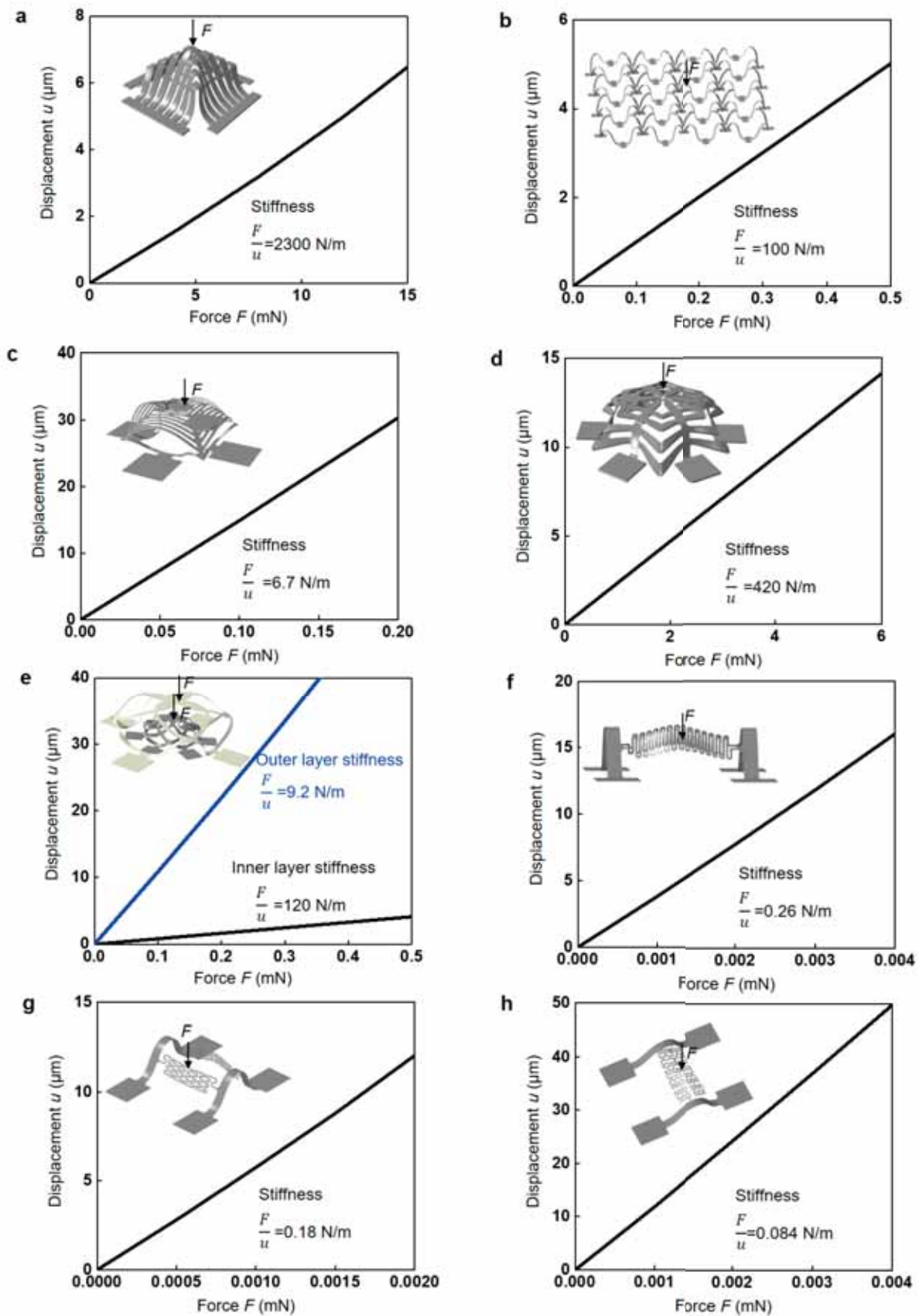
Supplementary Figure 4. SEM images of representative 3D filamentary mesostructures in PVDF. a, Bilayer cage. b, Triple-floor building. c, Double-floor network. d, 4 by 4 raised ring array. e, Table-tent mixed array. f, Peacock array. Scale bars, 500 μm .



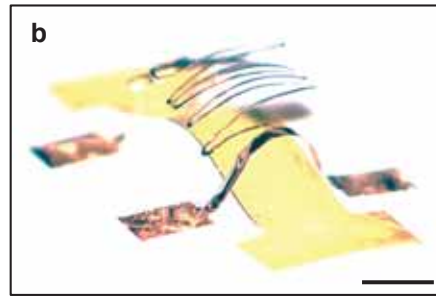
Supplementary Figure 5. SEM images of representative 3D mesostructures of membranes in PVDF. a, Kirigami-inspired butterfly. Scale bar, 500 μm . **b,** Origami-inspired football. Scale bar, 500 μm . **c,** Magnified view of the football structure. Scale bar, 100 μm .



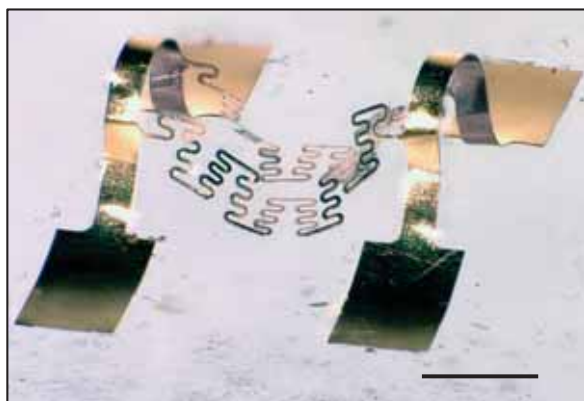
Supplementary Figure 6. 3D PVDF mesostructures with metal patterns. **a**, Optical image of a 3D serpentine structure. Scale bar, 2 mm. **b**, SEM image of the 3D serpentine structure with magnified view. Scale bar, 500 μm . **c**, SEM image of a jellyfish structure with metal patterns on top. Scale bar, 500 μm .



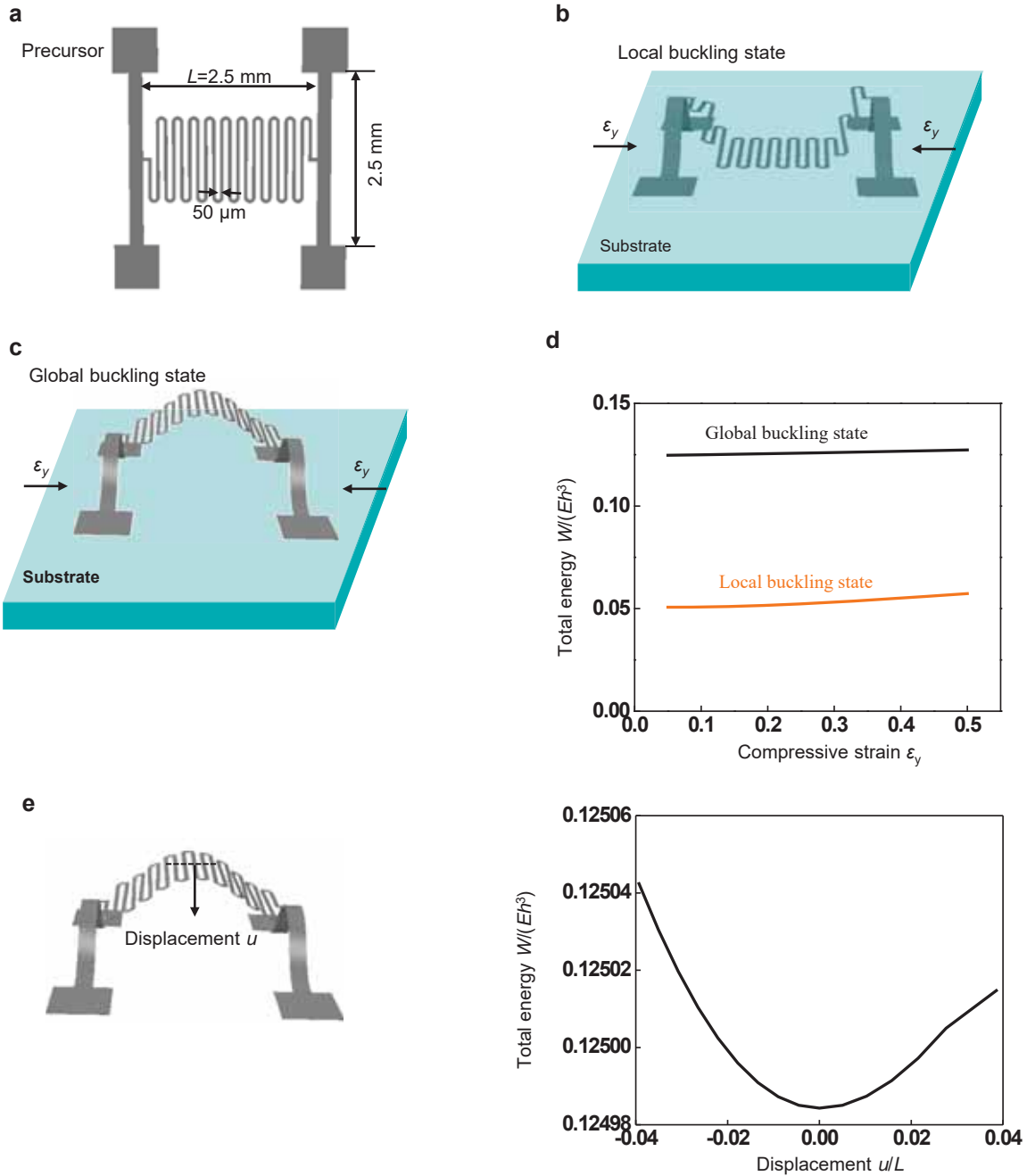
Supplementary Figure 7. FEA results of the relationship of displacement vs. force to illustrate the stiffness of the structures in Fig. 1. The stiffness of the serpentine structures (f-g) are at least one order of magnitude smaller than those of the conventional structures (a-e)



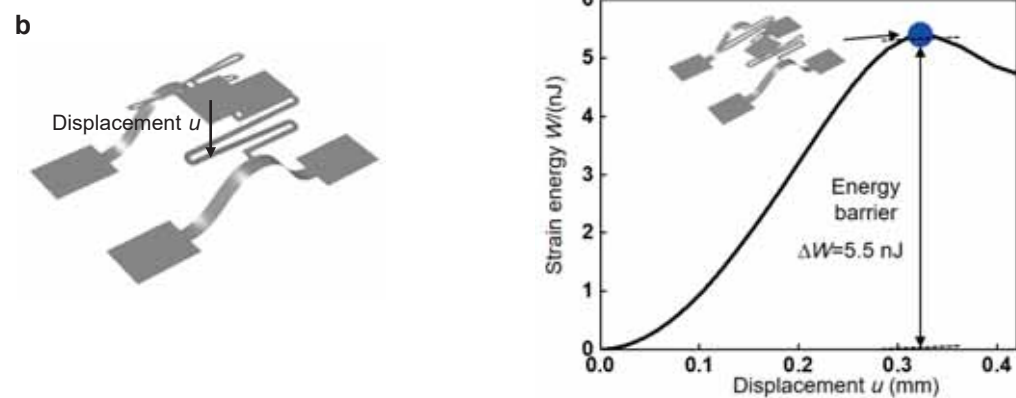
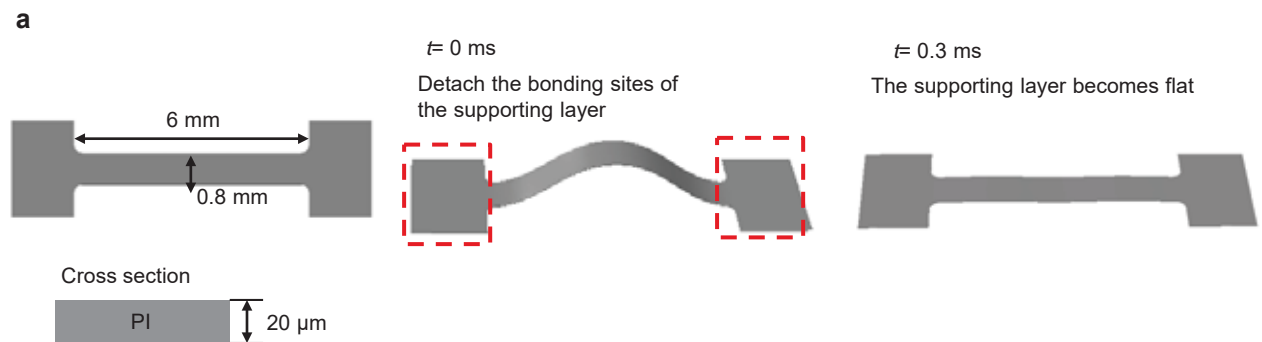
Supplementary Figure 8. Optical images of an ultra-low-stiffness 3D mesostructure. a, The ultra-low-stiffness 3D mesostructure with supporting layer. **b,** Separation of the supporting layer from the ultra-low-stiffness 3D mesostructure. Scale bars, 500 μm .



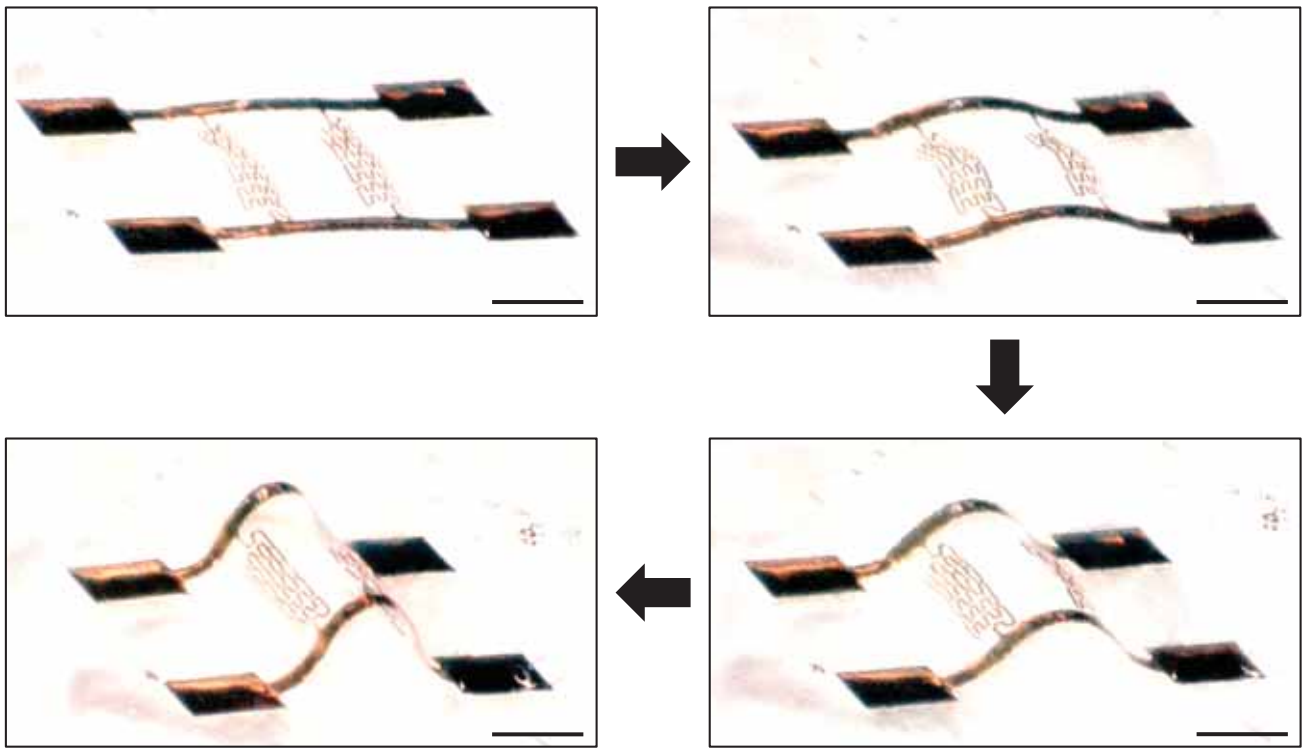
Supplementary Figure 9. Optical image of an ultra-low-stiffness serpentine buckled without temporary supporting layer. Scale bars, 500 μm .



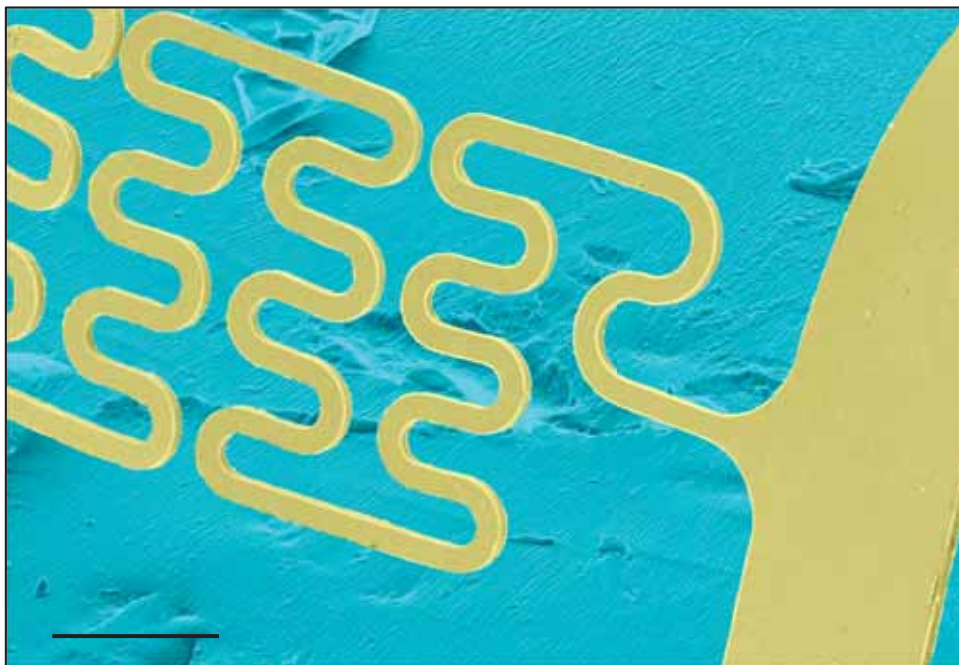
Supplementary Figure 10. A numerical example of the energetic analysis on the serpentine pattern. **a**, geometry of the 2D precursor. **b**, Local buckling state, in which the serpentine adheres to the substrate. **c**, Global buckling state, in which the serpentine buckles up. **d**, Total energy of the two states. **e**, Total energy vs. serpentine displacement measured from the global buckling state.



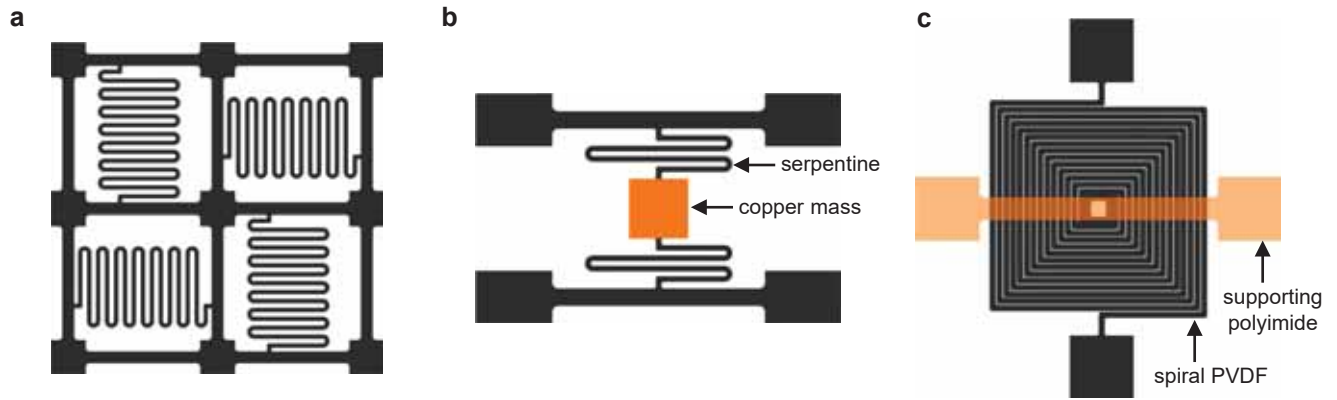
Supplementary Figure 11. a, FEA illustration of the deformation of the supporting layer after release from its bonding site. left frame: geometry of the 2D precursor; middle frame: at $t=0$ ms, release the bonding site; right frame: after 0.3 ms the supporting layer becomes flat. **b**. strain energy vs. serpentine displacement for the structure in Fig. 2e when it is pressed downwards.



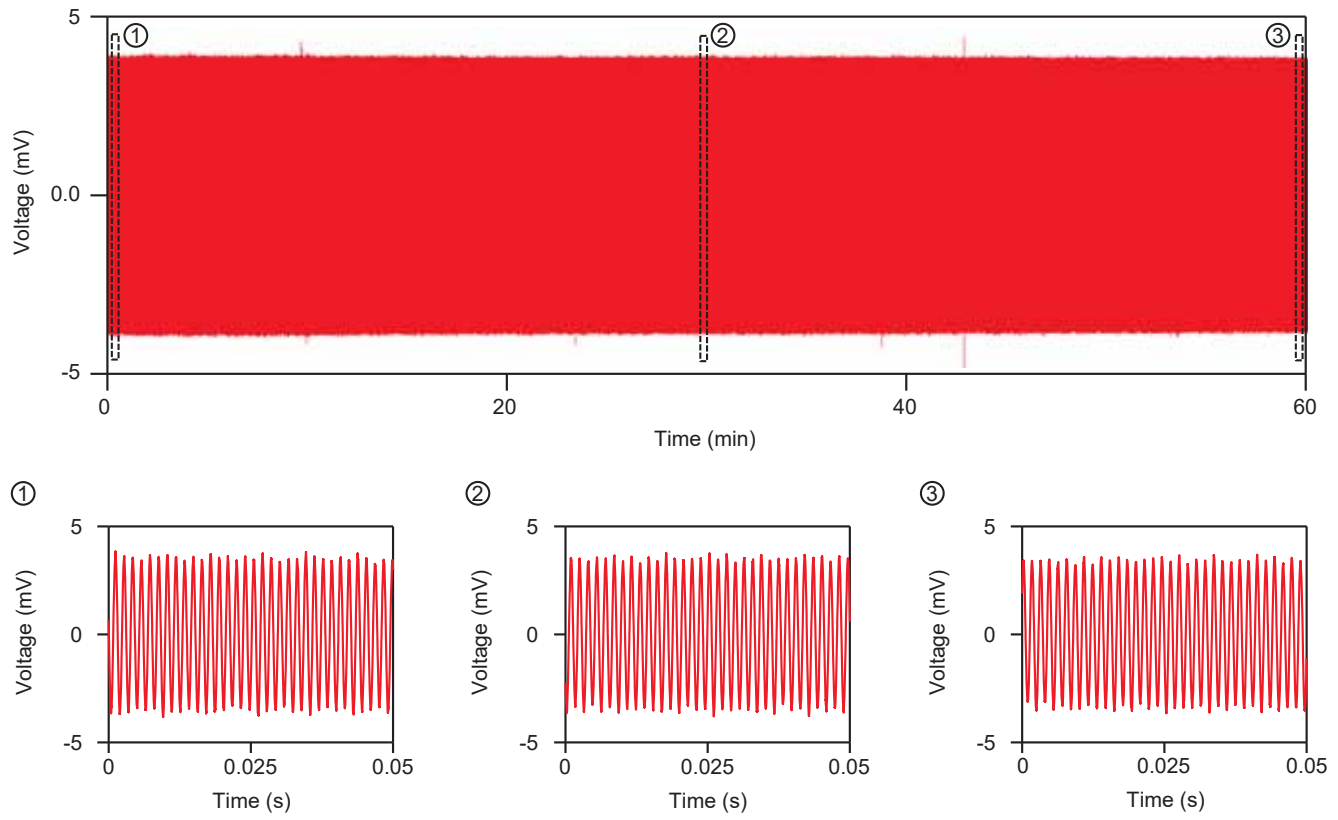
Supplementary Figure 12. Ultra-low-stiffness mesostructure switching between 2D and 3D geometries through stretching and releasing of the elastomer. Scale bars, 500 μm .



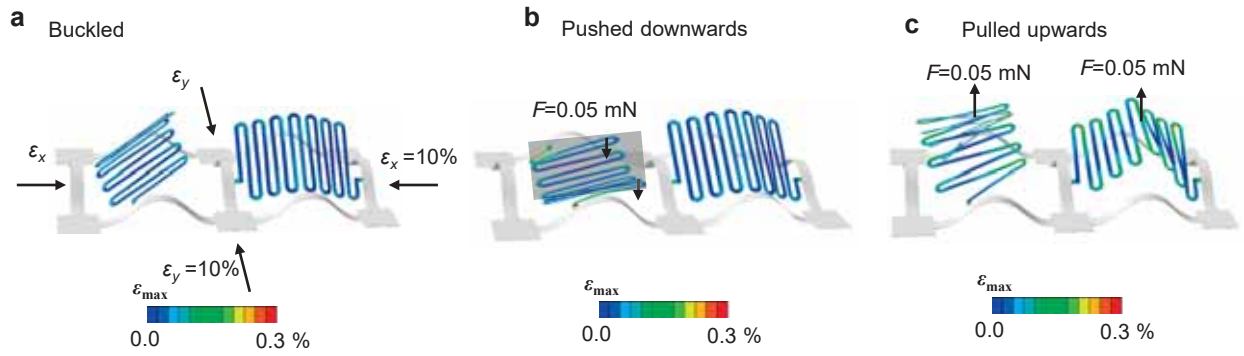
Supplementary Figure 13. Magnified SEM image of the two-order 3D fractal curve. Scale bars, 100 μm .



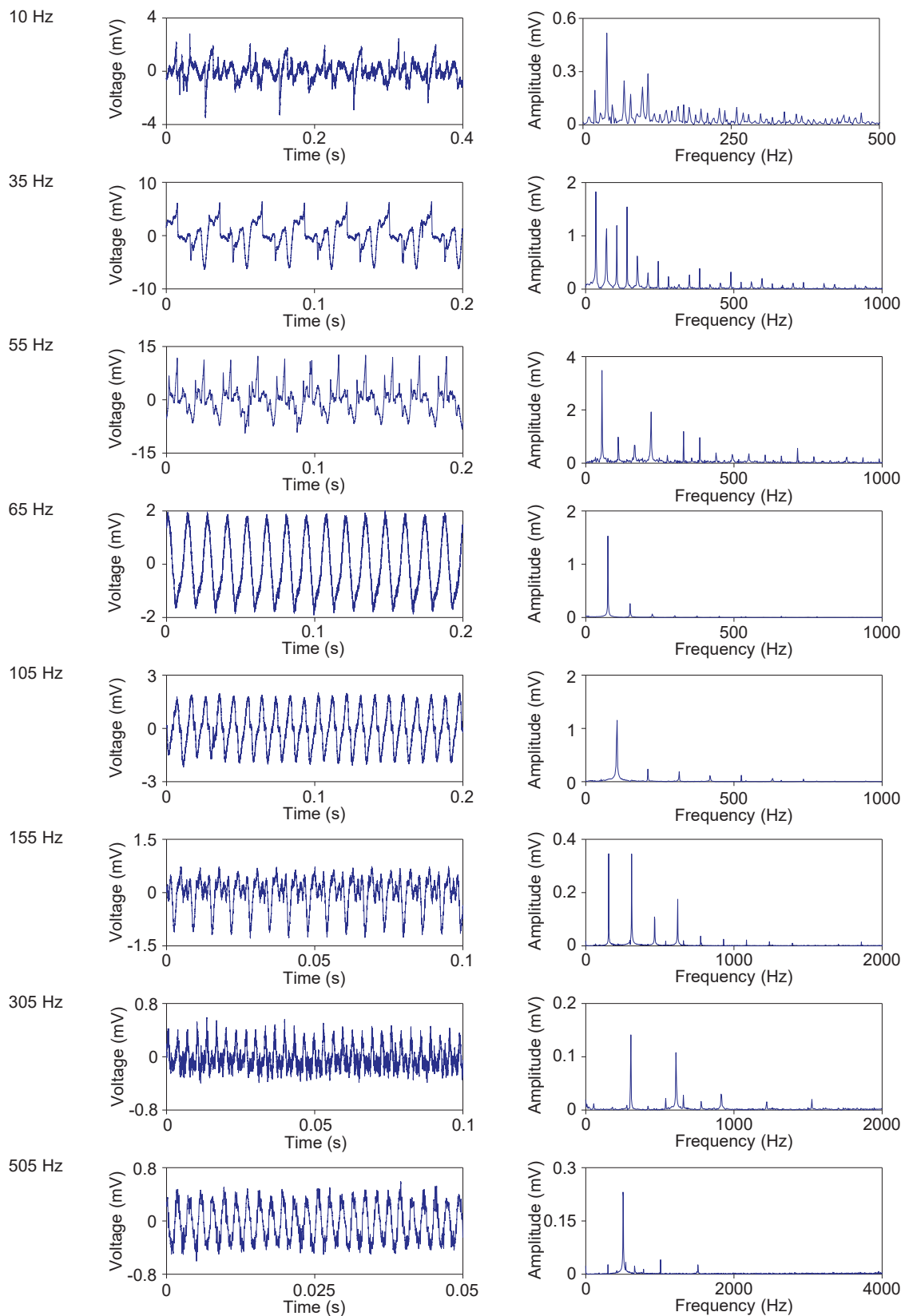
Supplementary Figure 14. 2D layouts of vibration-based energy harvesters. a, Array of 3D serpentes. **b,** Bi-stable 3D serpentine with copper mass. **c,** Multilayer 3D spiral structure.



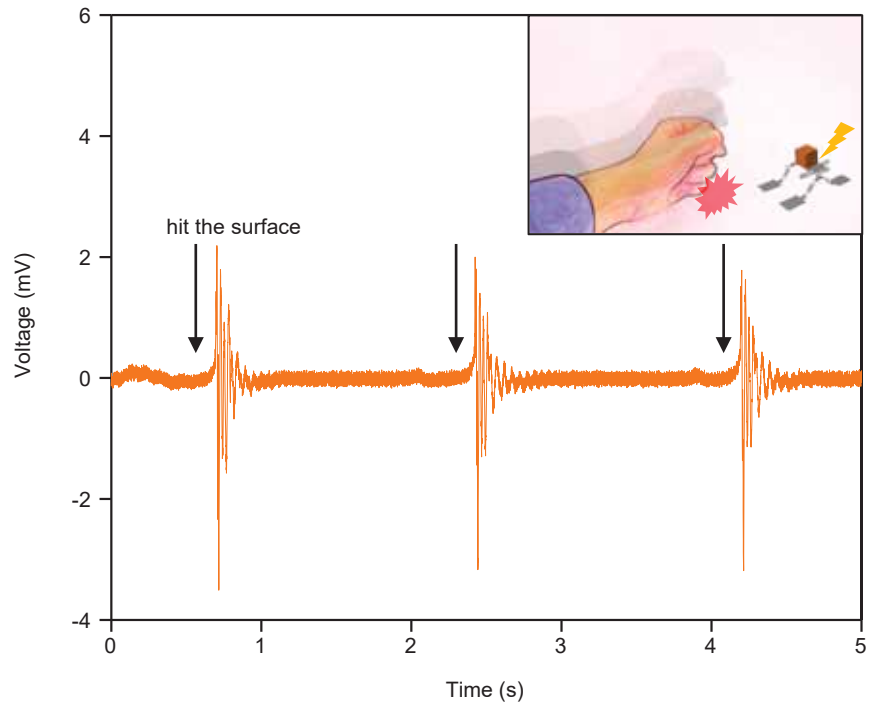
Supplementary Figure 15. Cyclic measurement of the 3D serpentine array under vibration with frequency of 657 Hz and acceleration of 4 g.



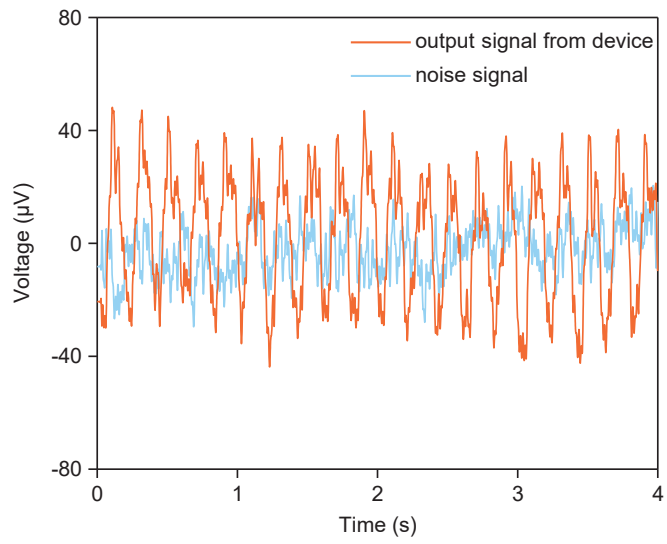
Supplementary Figure 16. Deformation and strain distribution of the 3D vibratory piezoelectric energy harvester (Fig. 2a). a-c, FEA result for the maximum principal strain in serpentine ribbons buckled by 10% compressive strain, pushed downwards by a 0.05 mN force and pulled upward by 0.05 mN force, respectively. In (b), the force is applied by pressing with a rigid plate. When the force exceeds 0.05 mN, the serpentine ribbon comes into contact with the underlying substrate.



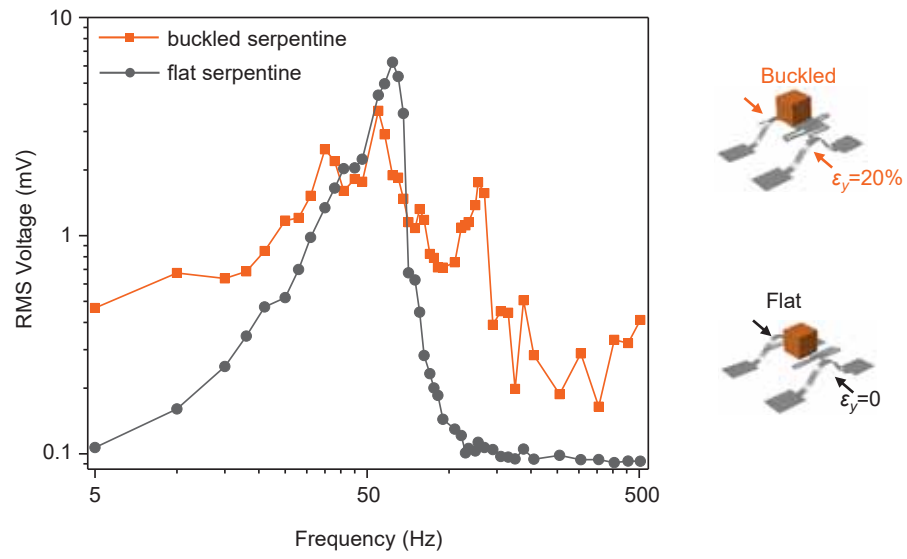
Supplementary Figure 17. Representative time-domain output voltage (left) and corresponding fast Fourier transform (right) of the 3D bi-stable serpentine with copper mass.



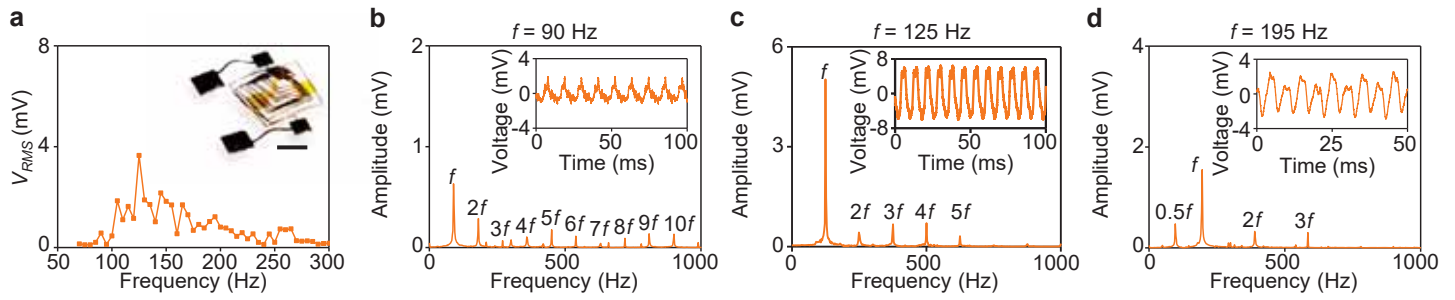
Supplementary Figure 18. Time-domain output voltage of the 3D bi-stable serpentine by periodically hitting the surface at a distance, with an inset that schematically illustrates the testing condition.



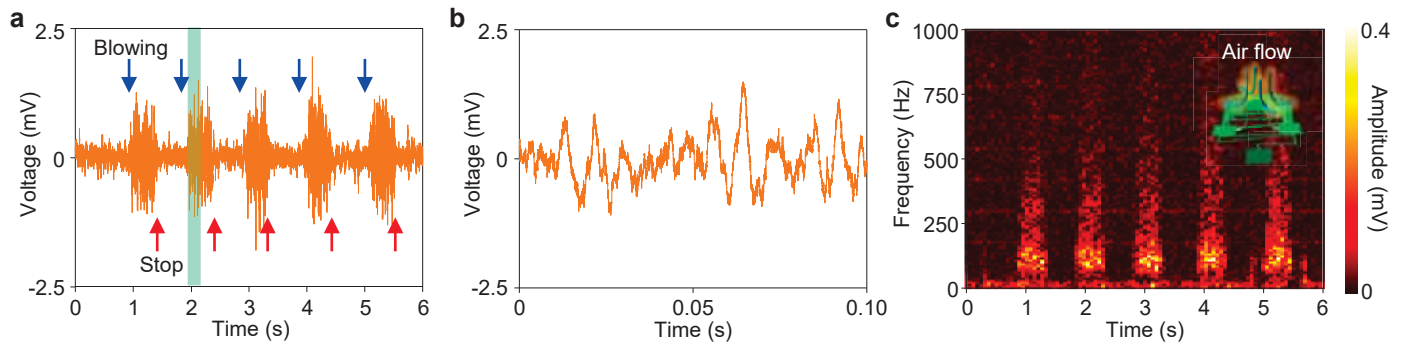
Supplementary Figure 19. Noise signal and output voltage of the bi-stable 3D serpentine structure with a low-pass (20 Hz) filter under vibration (frequency: 5 Hz, acceleration: 0.1 g).



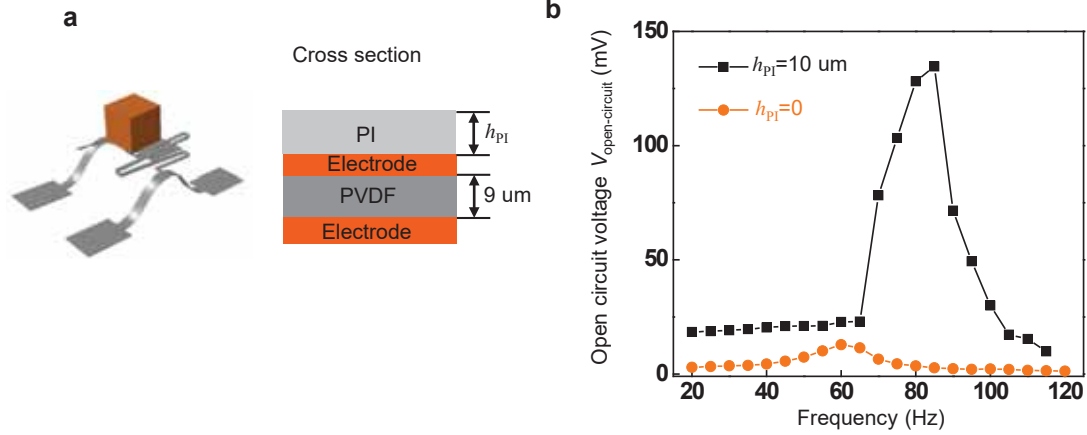
Supplementary Figure 20. RMS voltages of the 3D ultra-low-stiffness mesostructures with bi-stable serpentine and flat serpentine designs.



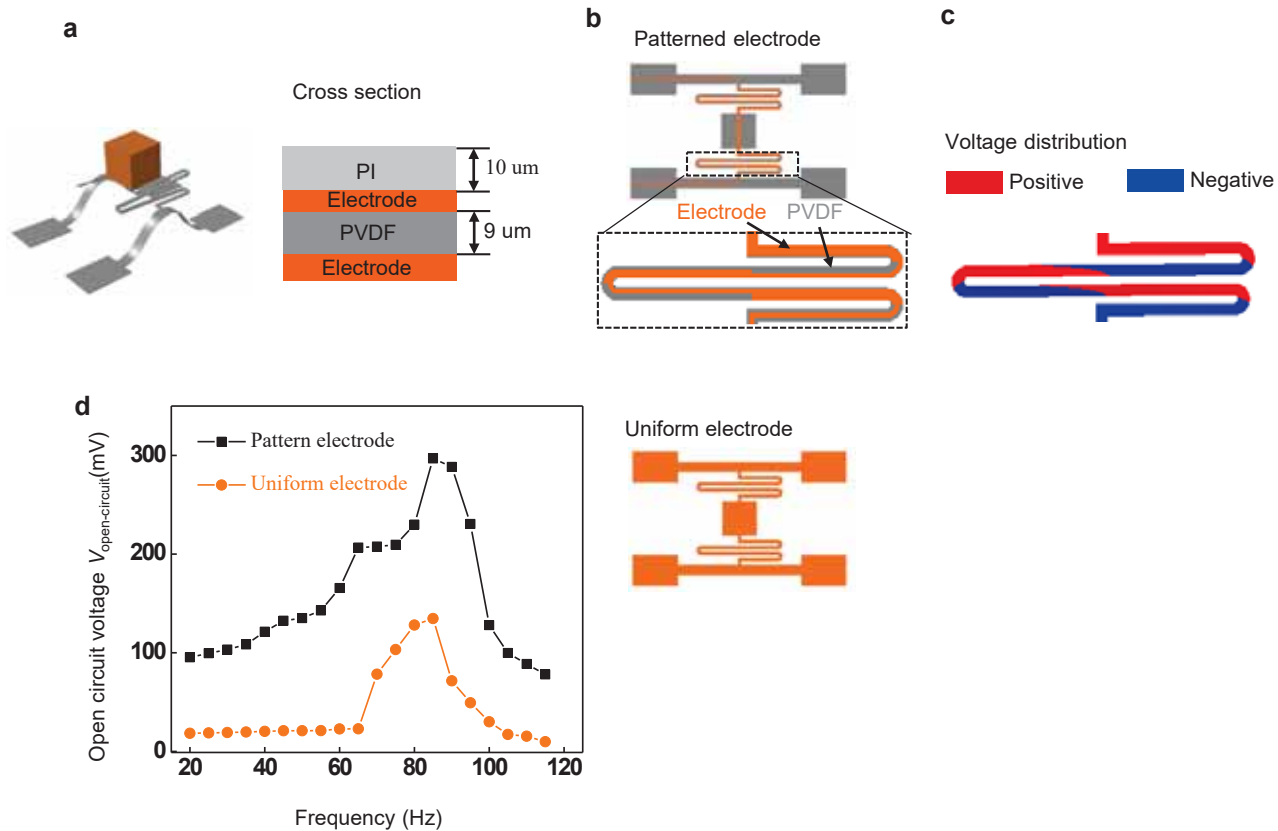
Supplementary Figure 21. Output of the 3D spiral structure. **a**, RMS voltage under different frequencies. Scale bar, 1 mm. **b-d**, fast Fourier transform at 90, 125 and 195 Hz, with insets show corresponding time-domain output voltage.



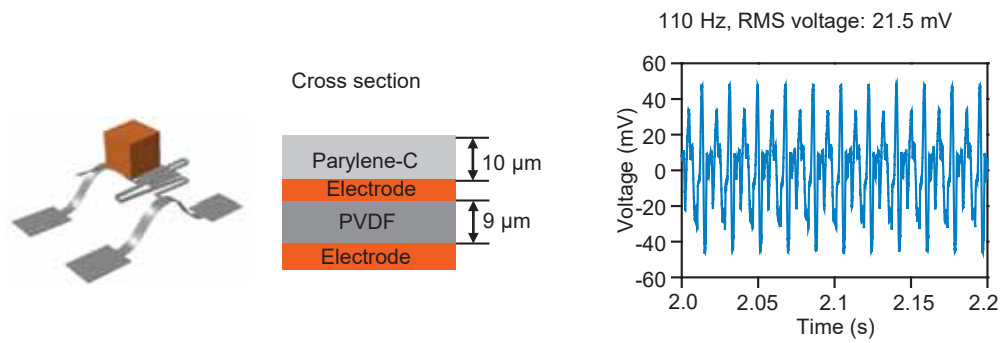
Supplementary Figure 22. Output of the 3D spiral structure from air flow. a, Time-domain output voltage. **b,** Magnified view of the output voltage. **c,** Spectrogram of the data shown in **a**, indicating a wide frequency range from 100 to 200 Hz.



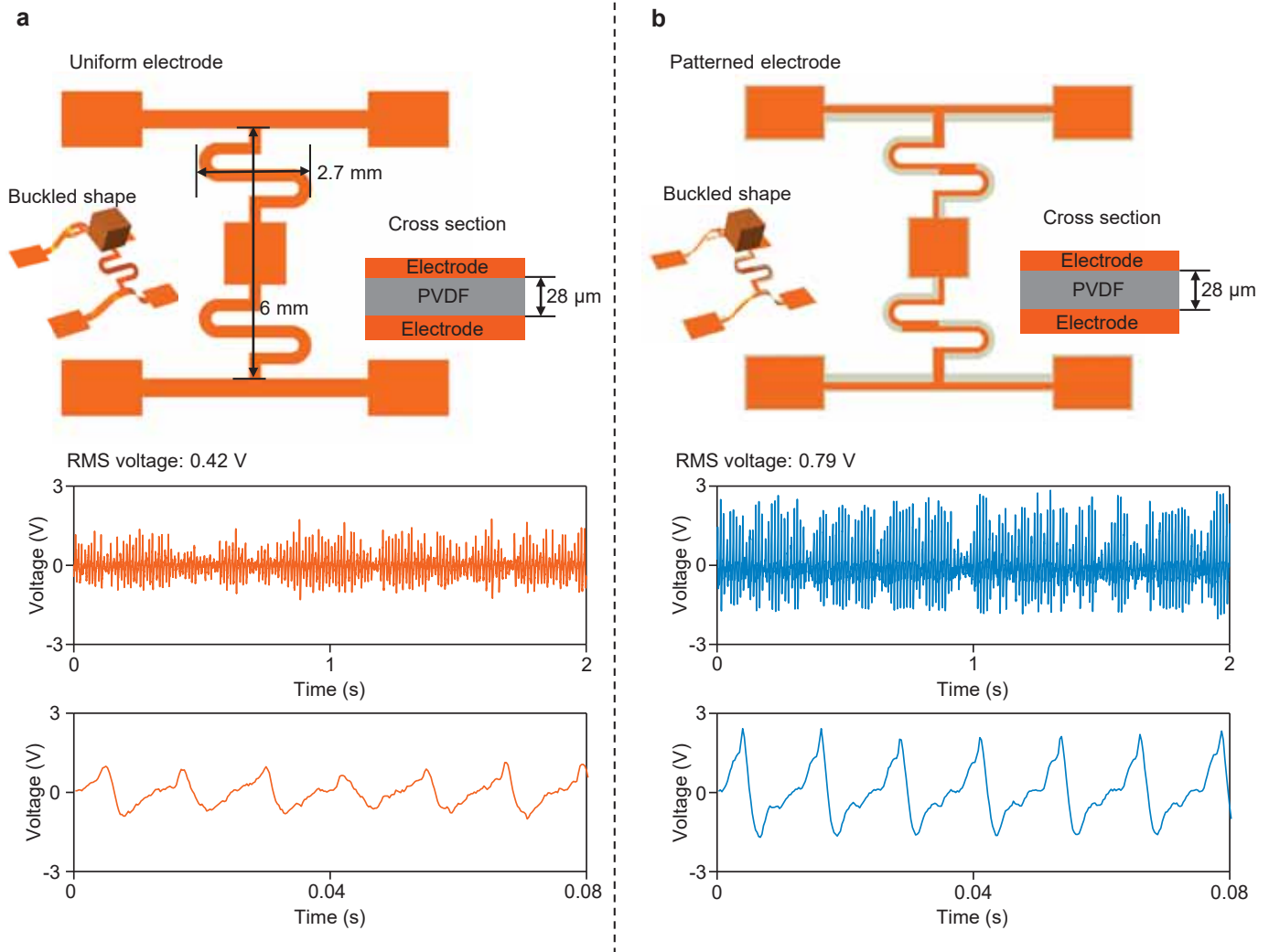
Supplementary Figure 23. Increase the output voltage by the supporting layer that offsets the PVDF from the neutral mechanical plane. a, 3D serpentine structure and its thickness profile. b, FEA result of the open-circuit output voltage (RMS).



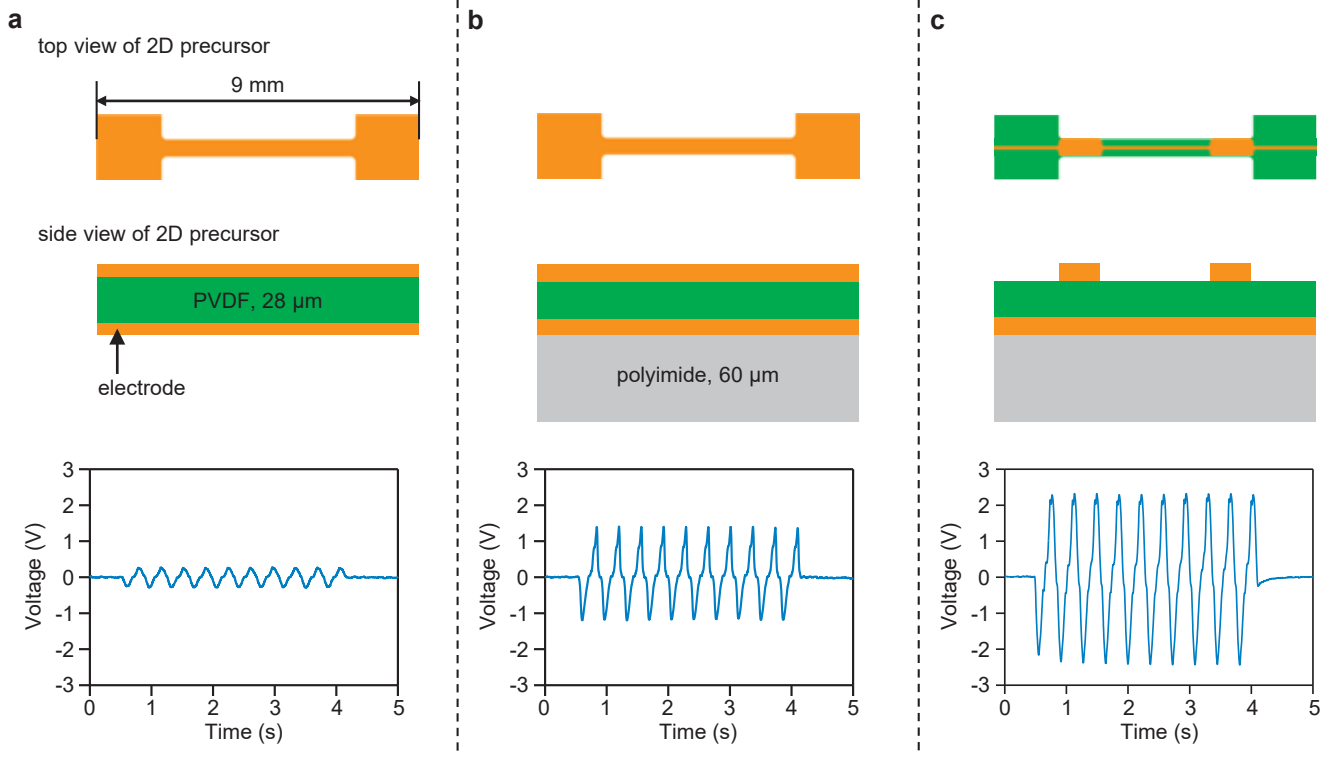
Supplementary Figure 24. Increase the output voltage by the patterned electrode. **a**, 3D serpentine structure and its thickness profile. **b**, Patterned electrode. **c**, FEA result of the voltage distribution without the electrode. **d**, FEA result of the open-circuit output voltage (RMS).



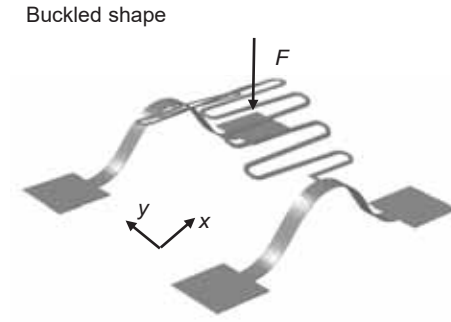
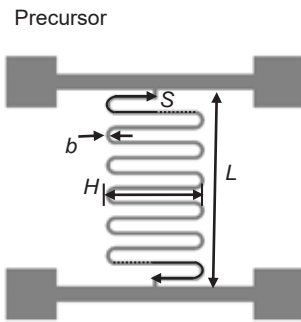
Supplementary Figure 25. Output voltages of the 3D vibratory energy harvester in Fig. 2e with a supporting layer to offset the neutral mechanical plane. At 110 Hz, the RMS voltage is 21.5 mV. In comparison, the largest RMS voltage for the energy harvester without the supporting layer is 4 mV (Fig. 2e) for the frequency in the range of 5-500 Hz.



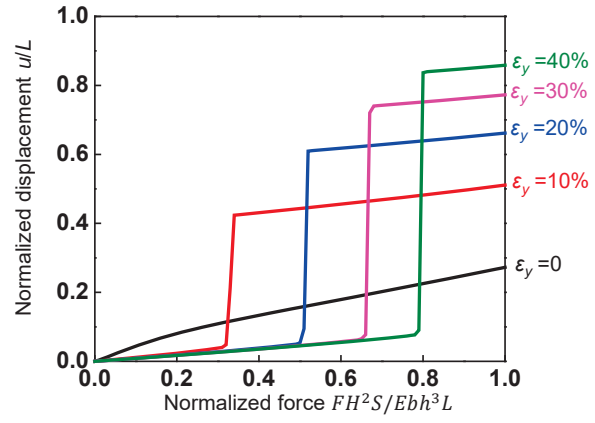
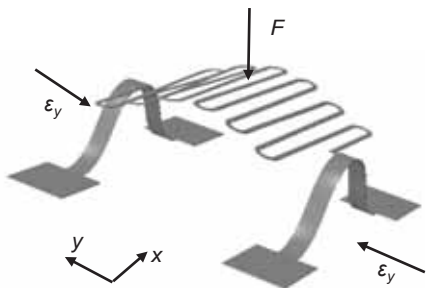
Supplementary Figure 26. Output voltages at 100 MΩ for the 3D serpentine structure during vibration (frequency: 80 Hz, acceleration: 4 g) to illustrate the effect of the patterned electrode. Schematic illustrations and output voltages of the structures with uniform electrode (a), and patterned electrode (b). The intermittent oscillations in the time-domain responses indicate nonlinear vibrations.



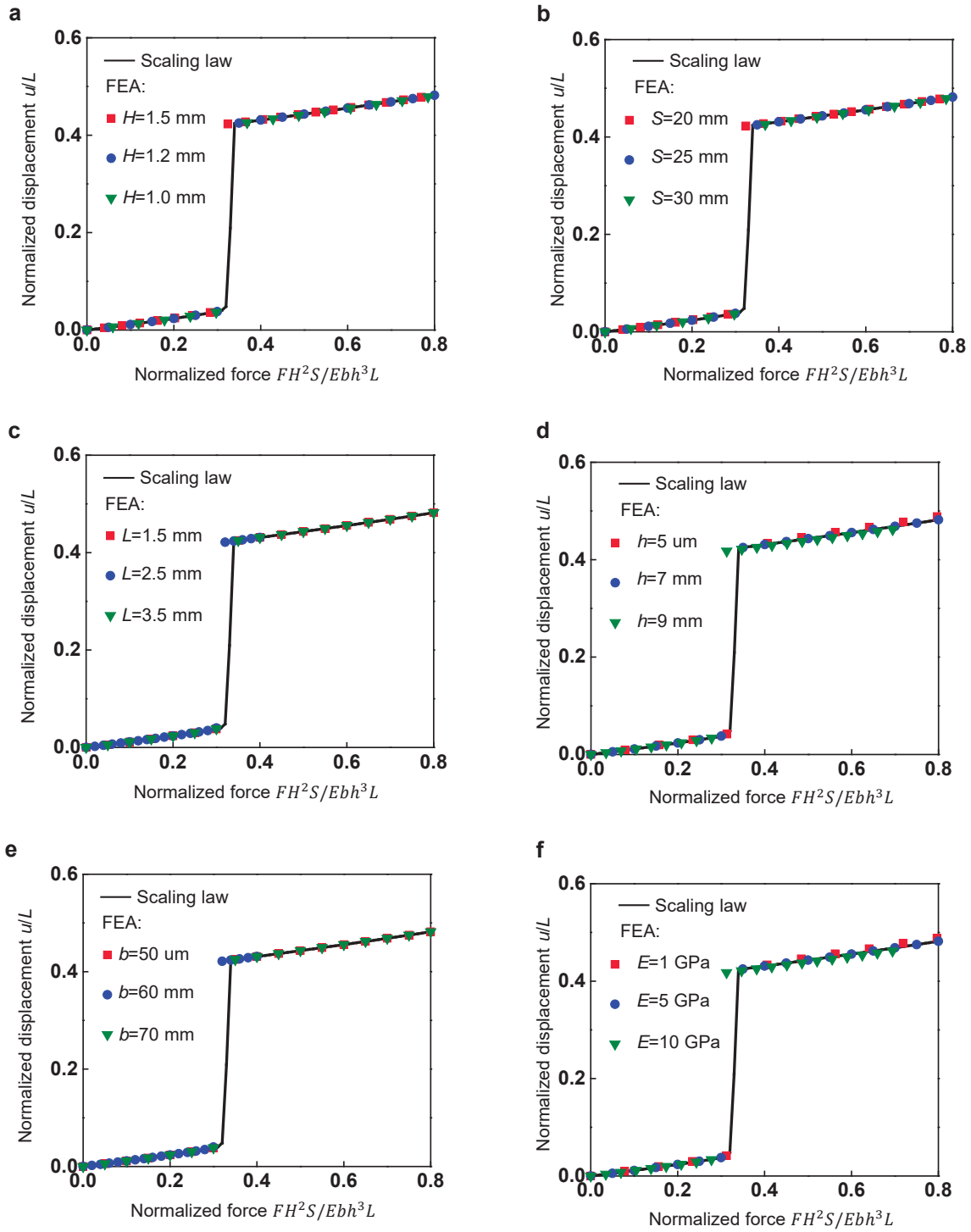
Supplementary Figure 27. Output voltages of 3D piezoelectric ribbons with periodic 10% tensile strain. a, Output voltage of a 3D piezoelectric ribbon. **b,** Output voltage of a 3D piezoelectric ribbon with supporting layer. **c,** Output voltage of a 3D piezoelectric ribbon with supporting layer and patterned electrode.



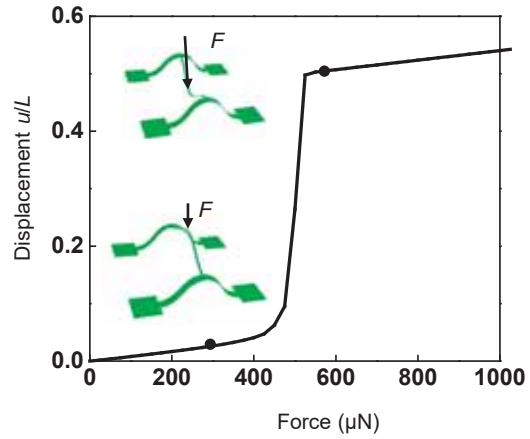
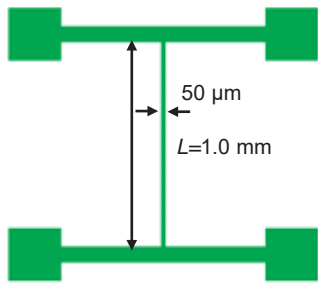
Supplementary Figure 28. Proof-of-concept design of the serpentine pattern with variable geometry parameters for the fundamental study of the broadband and low frequency energy harvester.



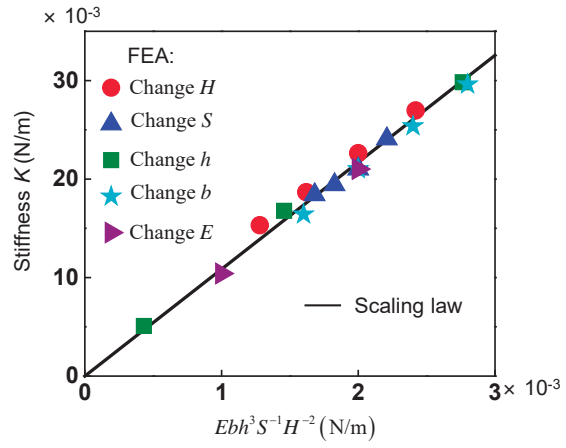
Supplementary Figure 29. Normalized displacement vs. normalized force curve for the serpentine pattern buckled by the compressive strain ranging from 0 to 40%.



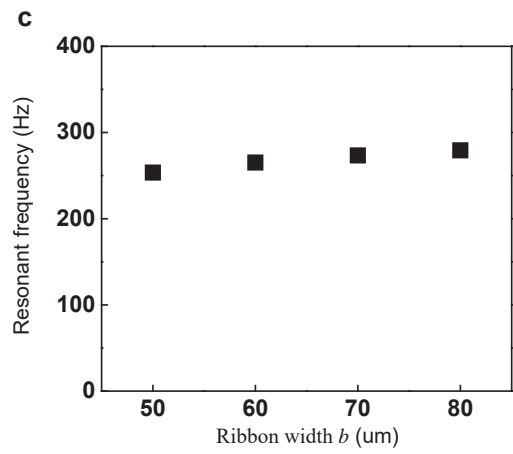
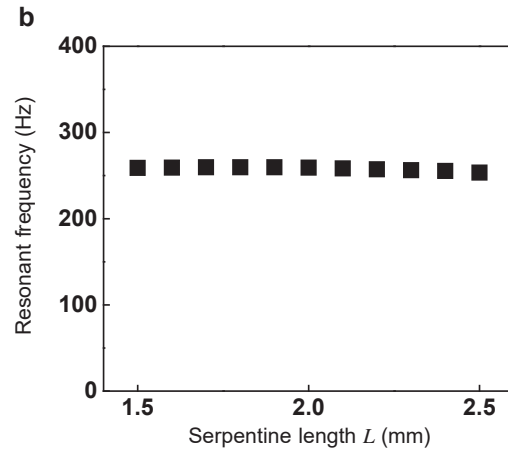
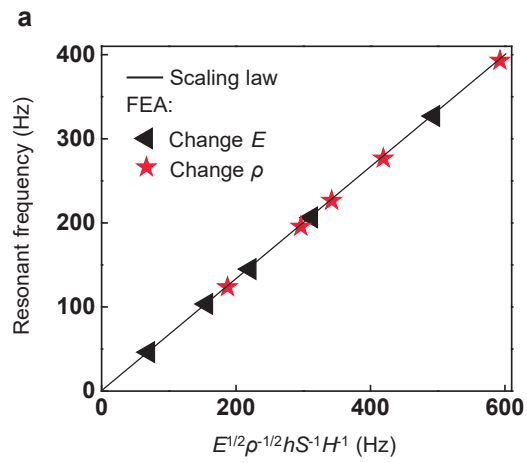
Supplementary Figure 30. FEA validation of the scaling law Eq. (1). The normalized displacement vs. normalized force curve for various **a**, Serpentine height H . **b**, Total serpentine arch length. **c**, Serpentine length L . **d**, Thickness h . **e**, Serpentine width b . **f**, Young's modulus E .



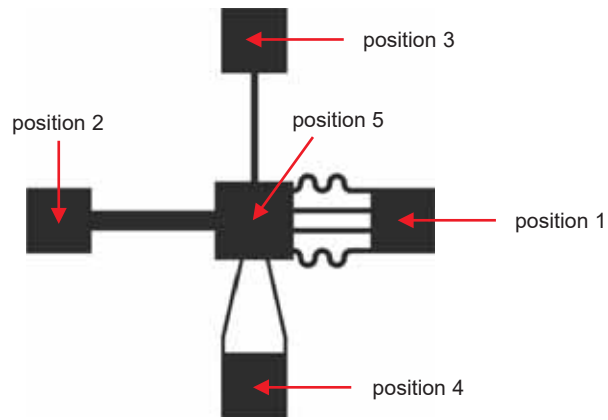
Supplementary Figure 31. The displacement vs. force curve for a straight ribbon. The straight ribbon structure requires 500 μN force to actuate nonlinear deformation. By comparison, a serpentine structure with otherwise similar geometries and materials requires only 2 μN to actuate nonlinear deformation, as the scaling law Eq. (1) (Fig. 2k) suggests.



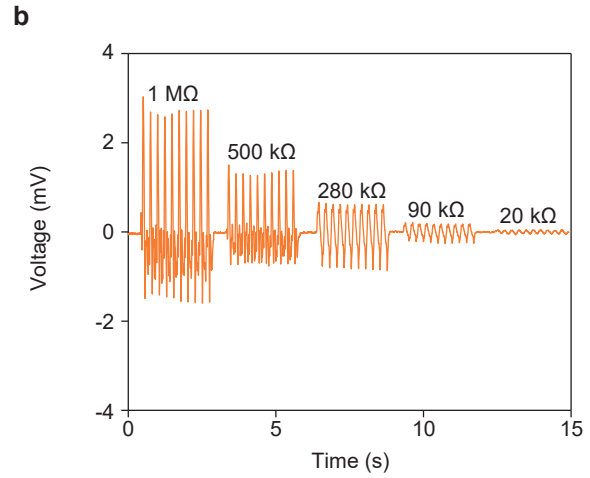
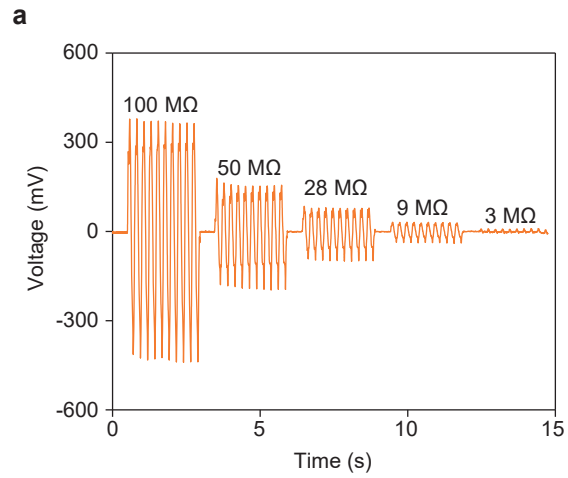
Supplementary Figure 32. FEA validation of the scaling law for serpentine stiffness



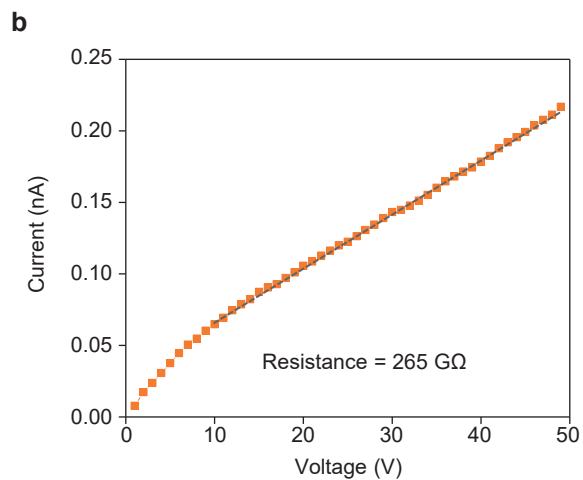
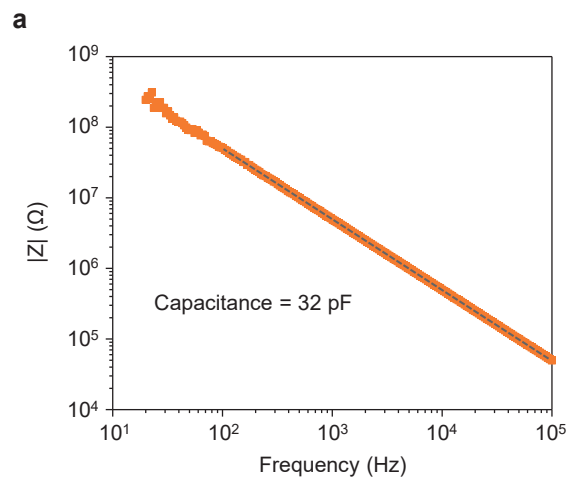
Supplementary Figure 33. FEA result of the variation of the resonant frequency with a, Young's modulus E and density ρ . b, serpentine length L and c, ribbon width b .



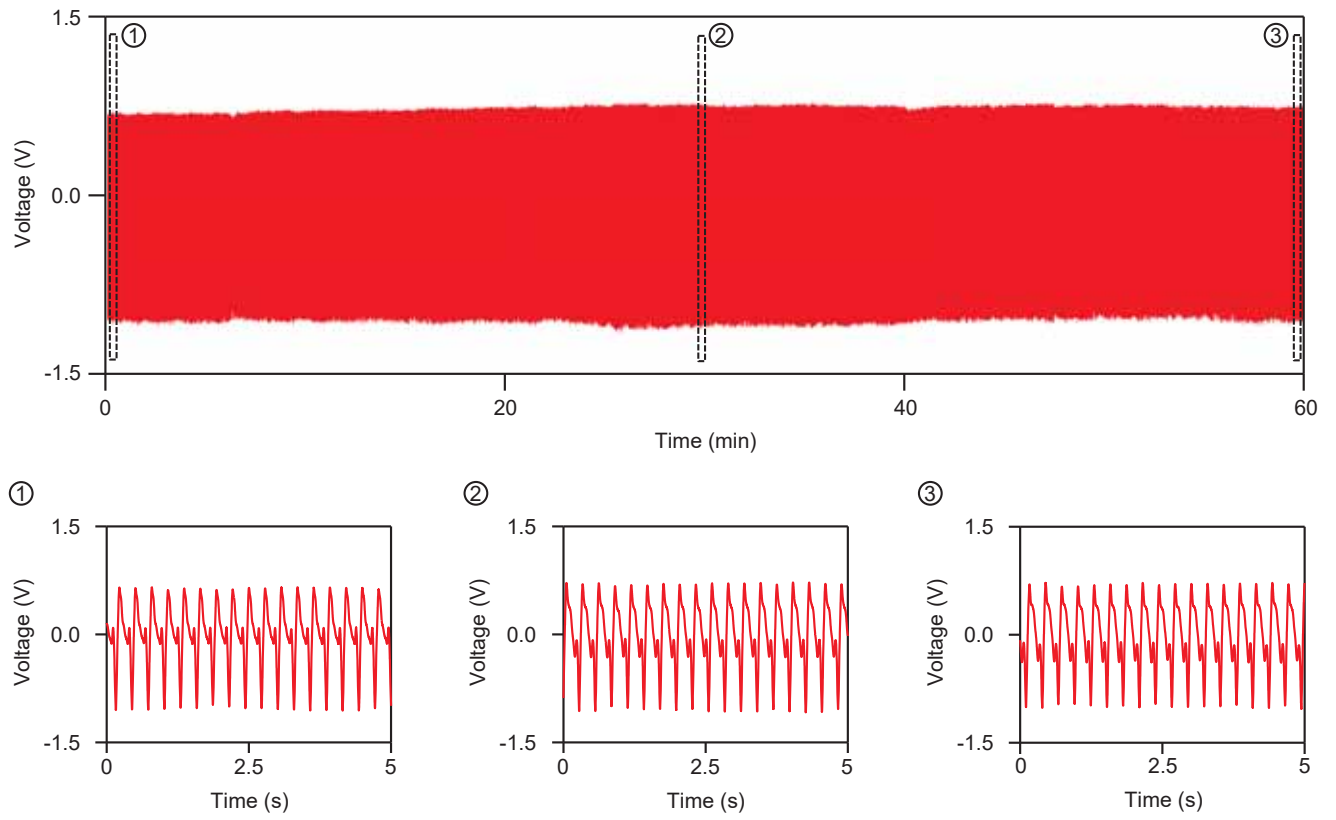
Supplementary Figure 34. 2D layout of impact-based energy harvester.



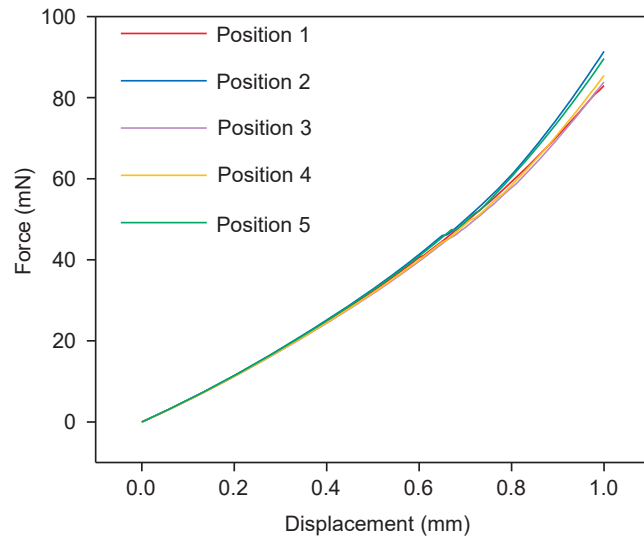
Supplementary Figure 35. Time-domain output voltage of 3D piezoelectric device under different resistances. a, Output from 100 MΩ to 3 MΩ. **b,** Output from 1 MΩ to 20 kΩ.



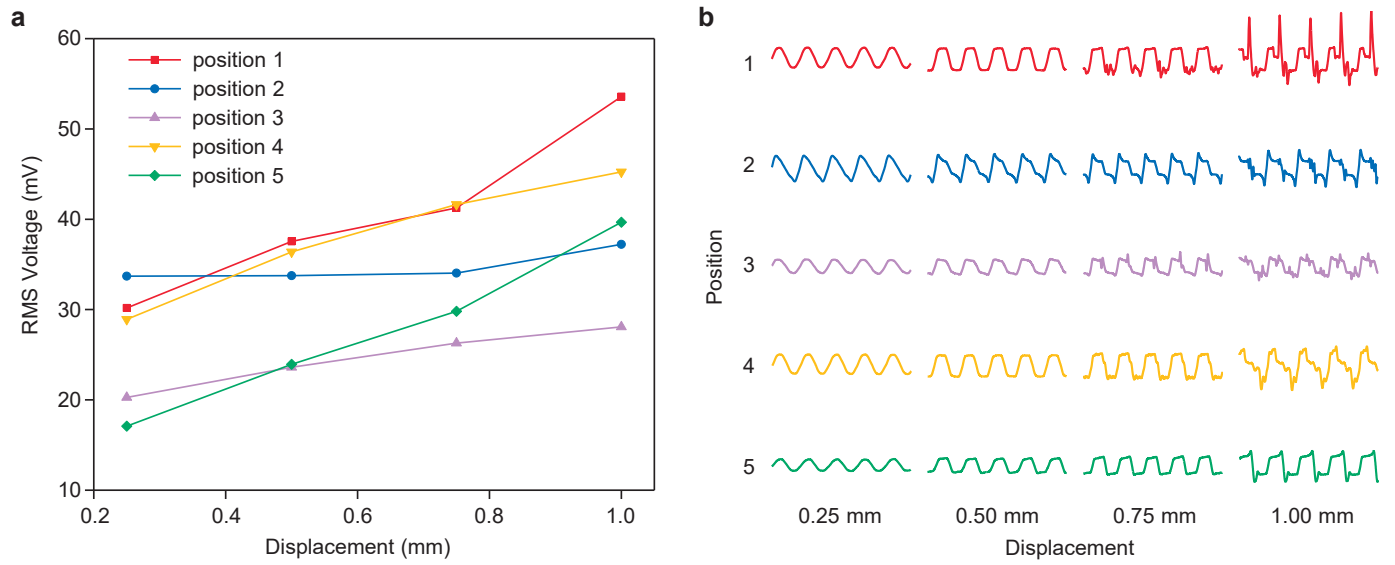
Supplementary Figure 36. Impedance of the 3D piezoelectric device. a, Magnitude of impedance from 20 to 100 kHz, indicating an equivalent capacitance of 32 pF. **b,** I-V curve, indicating an equivalent resistance of 265 G Ω .



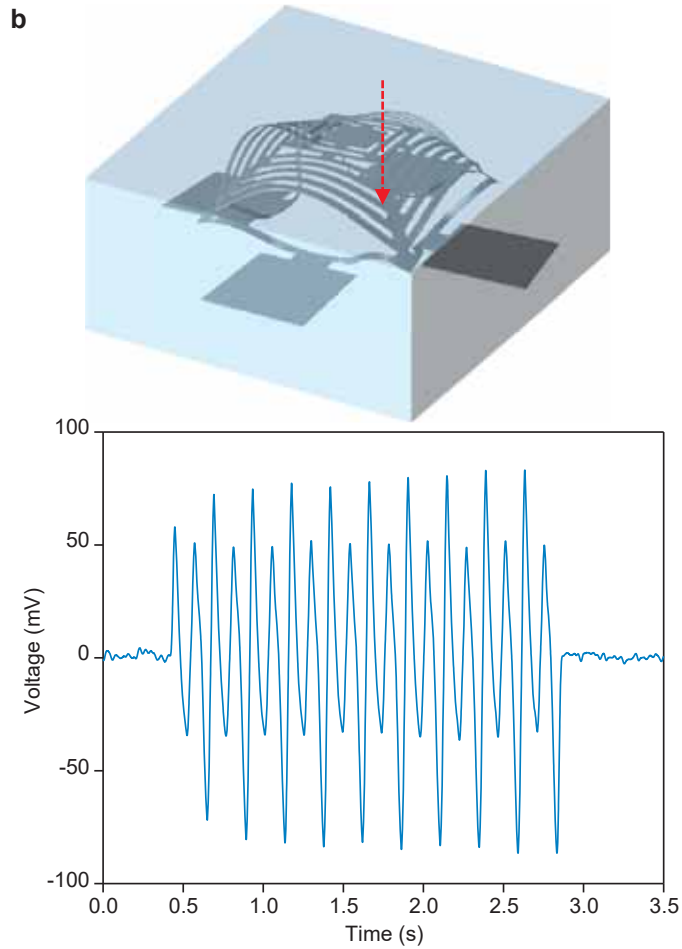
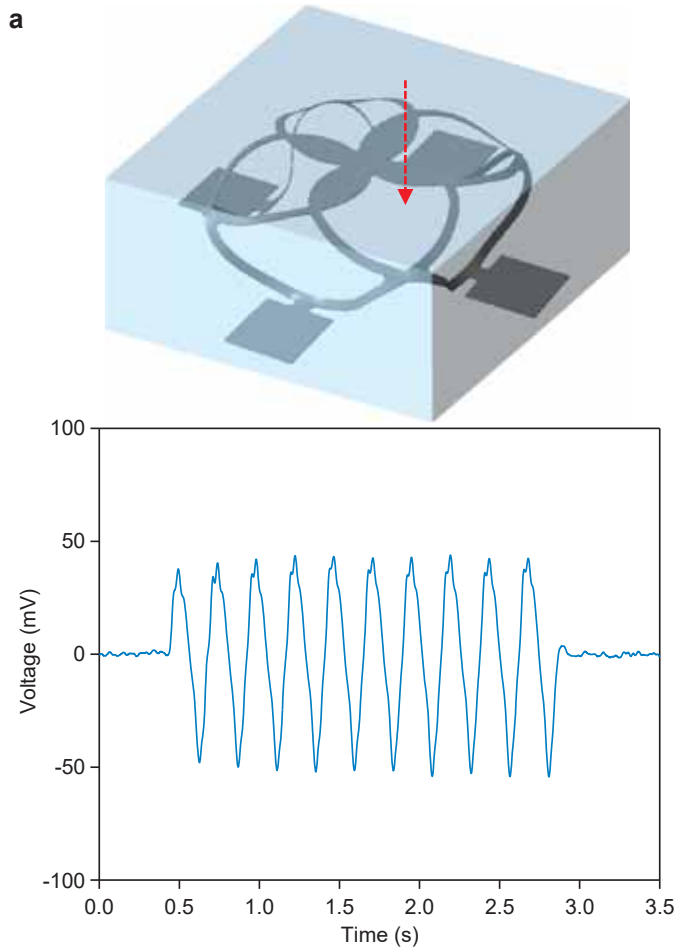
Supplementary Figure 37. Cyclic measurement of the impact-based 3D piezoelectric energy harvester under pressing with normal force of 32 N.



Supplementary Figure 38. FEA results of the relationship of displacement vs. force when applying force on the impact-based 3D piezoelectric device over a circular region with diameter of 0.65 mm.

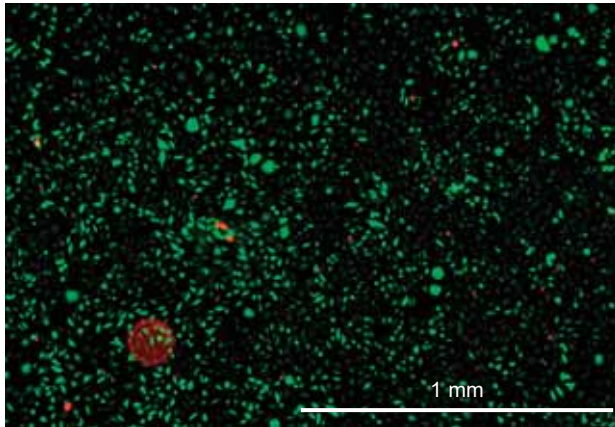


Supplementary Figure 39. Output voltage of the 3D piezoelectric device with external forces applied over different small circular regions. a, RMS voltages at different pressing positions and displacements. **b,** Time-domain response shapes at different pressing positions and displacements.

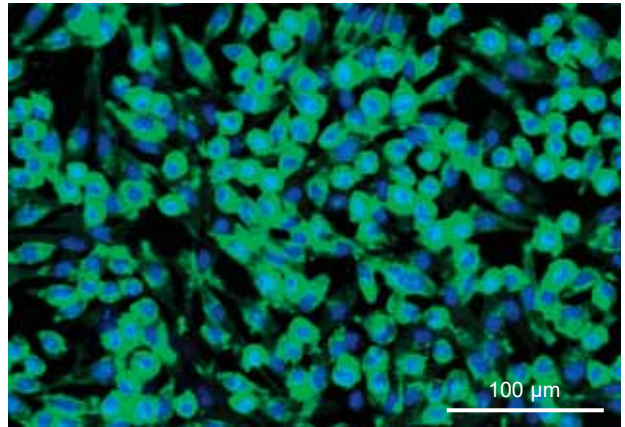


Supplementary Figure 40. Output voltages of different 3D piezoelectric mesostructures with external forces applied over small circular regions (0.65 mm in diameter). a, 3D mesostructure of filamentary components. b, 3D mesostructure of mixed membranes and filaments.

a



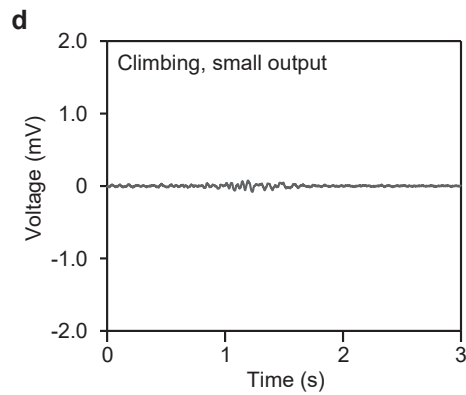
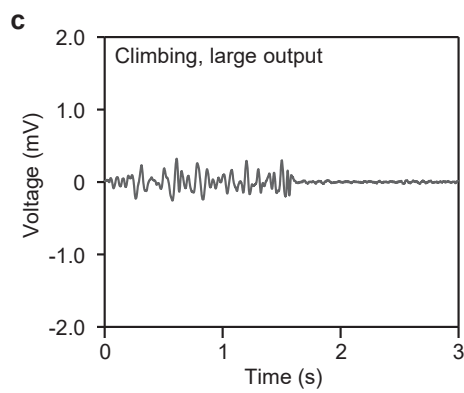
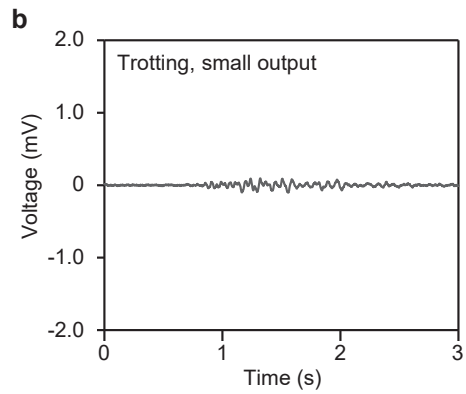
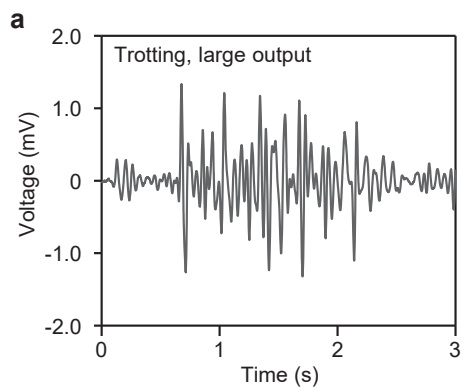
b



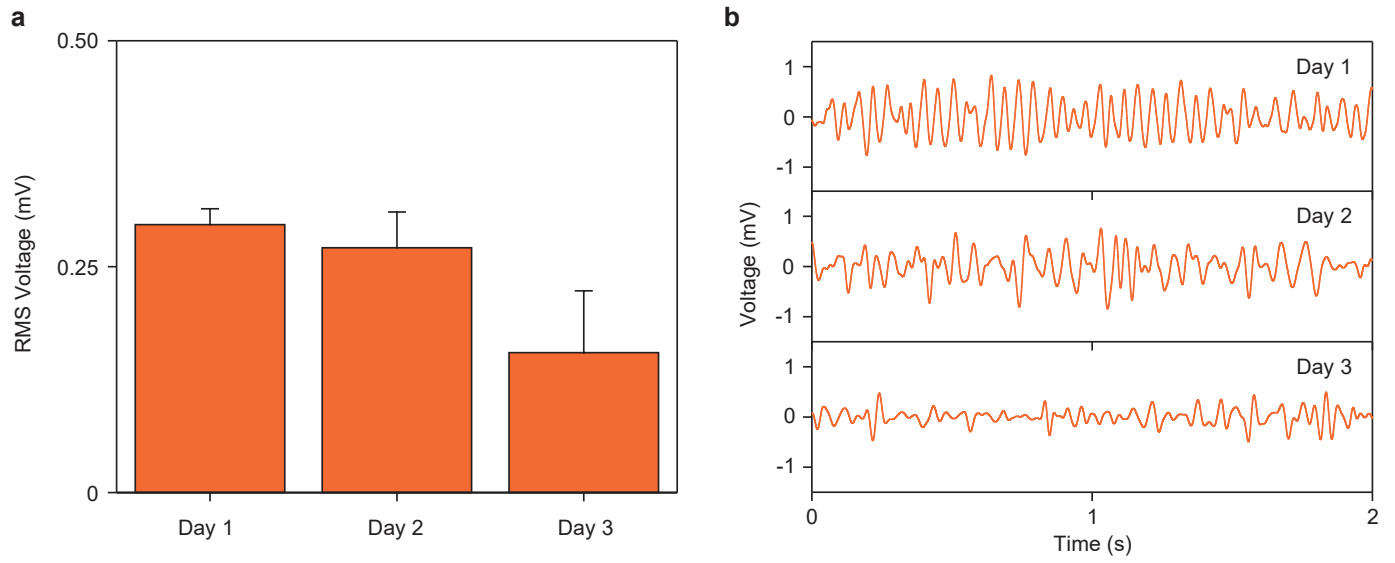
Supplementary Figure 41. Representative fluorescent images of fibroblast cultured on tissue culture plastic. a, Cytotoxicity assay (live/dead test) after 3 days of culturing. Green indicates live cells and red indicates dead cells. **b,** F-actin staining after 7 days of culturing. Green indicates actin filaments and blue indicates cell nuclei.



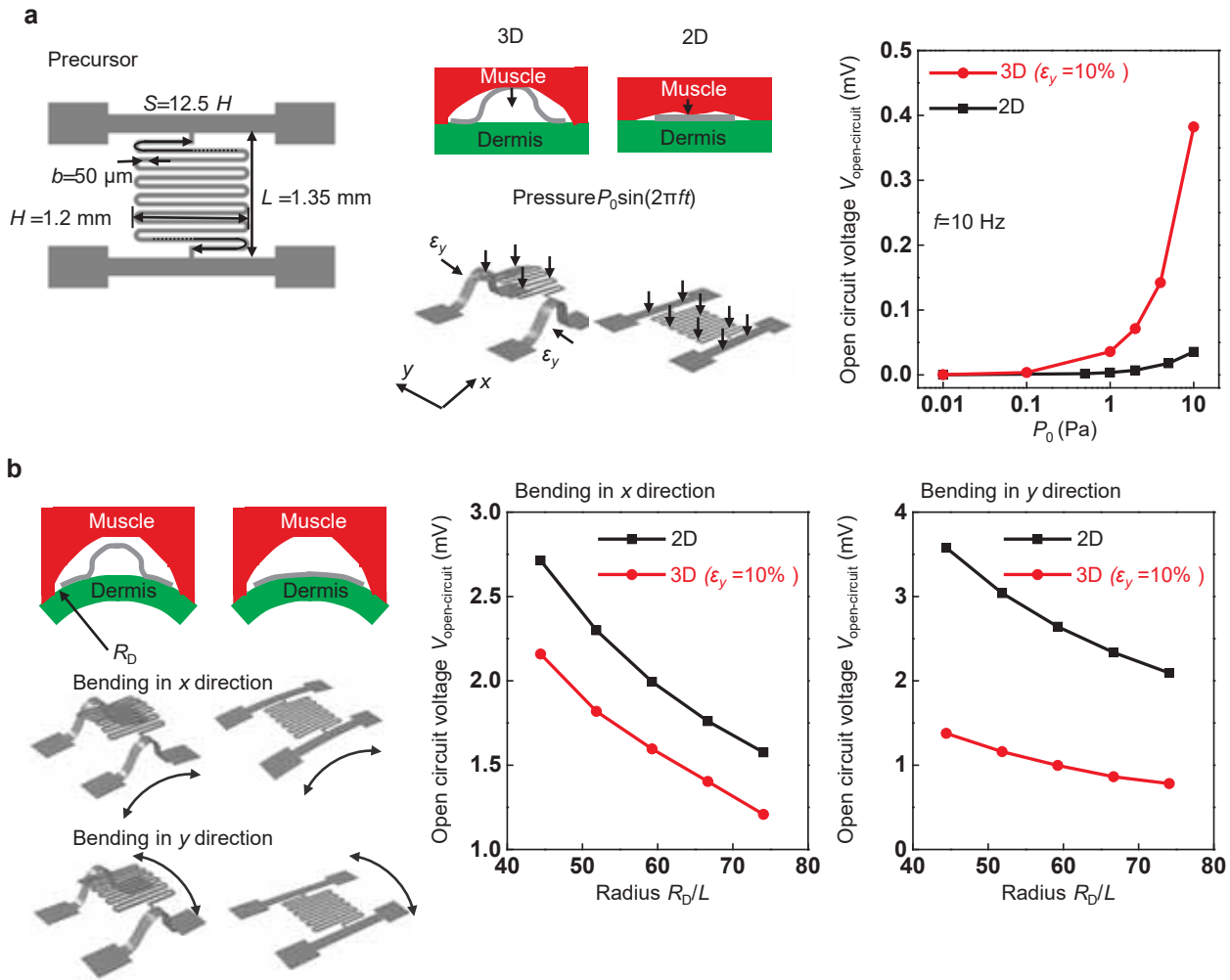
Supplementary Figure 42. Layout of the 2D precursor for subdermal implantation.



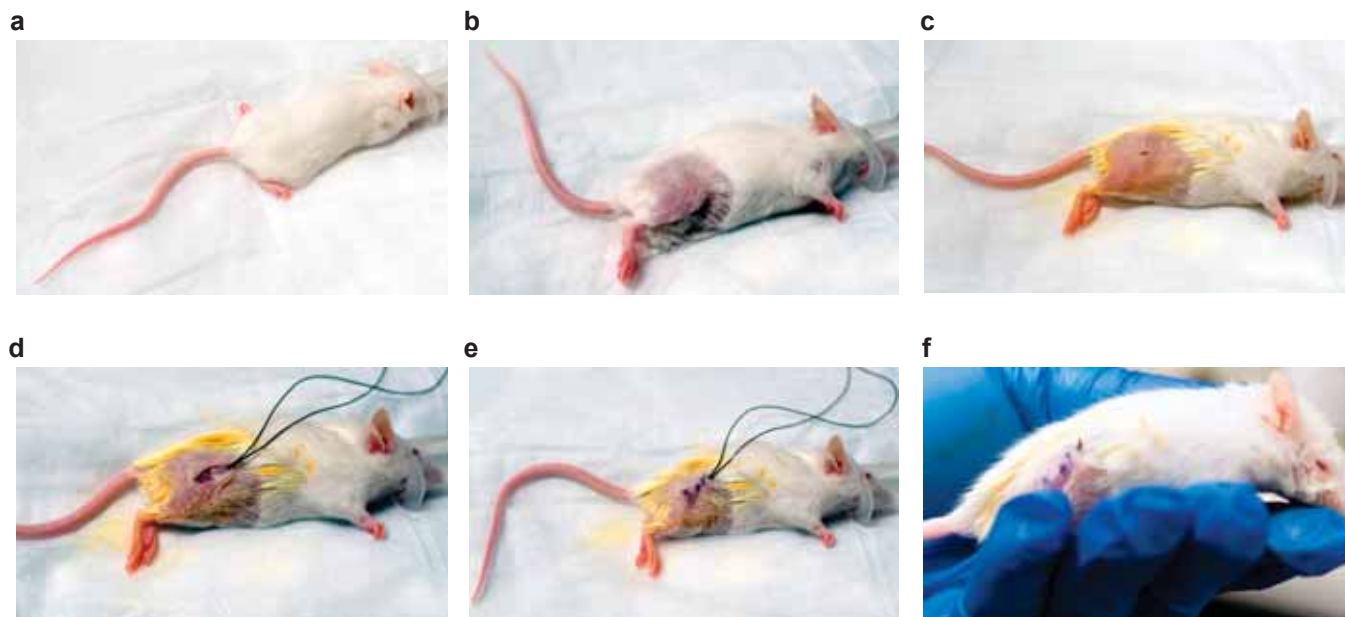
Supplementary Figure 43. Time domain output voltage from the implanted 2D precursor.



Supplementary Figure 44. Output voltages from the implanted piezoelectric device under trotting behaviors. a, RMS voltages from day 1 to day 3. Data correspond to averages of 5 different trotting behaviors. **b,** Time-domain output voltages from day 1 to day 3.



Supplementary Figure 45. a, FEA result of the open-circuit output voltage (RMS) of the 3D structure when the muscle pushes from the top, compared with that of the 2D precursor. Dermis modulus: 100 kPa. **b**, FEA result of the open-circuit output voltage (RMS) of the 3D structure under bending, compared with that of the 2D precursor.



Supplementary Figure 46. Surgical procedure. **a**, Anaesthetizing with isoflurane gas. **b**, Fur removal. **c**, Surgical exposure. **d**, Insertion of a 3D energy harvester into the subcutaneous region. **e**, Suturing and gluing. **f**, Mouse with implanted 3D energy harvester after surgery.